Cordierite under hydrostatic compression: Anomalous elastic behavior as a precursor for a pressure-induced phase transition (REVISION 1b)

Ronald Miletich[1], G. Diego Gatta[2], Thomas Willi[3,*], Peter W. Mirwald[4], Paolo Lotti[2], Marco Merlini[2], Nicola Rotiroti[2], and Thomas Loerting[5]

[1] Institut für Mineralogie und Kristallographie, Universität Wien, Althanstrasse 14, A-1090 Wien, Austria

[2] Dipartimento di Scienze della Terra, Università degli Studi di Milano, Via Botticelli 23, I-20133 Milano, Italy

[3] Institut für Geowissenschaften, Universität Heidelberg, Im Neuenheimer Feld 234-236, D-69120 Heidelberg, Germany

[4] Institut für Mineralogie und Petrographie, Universität Innsbruck, Innrain 52, A-6020 Innsbruck, Austria

[5] Institut für Physikalische Chemie, Universität Innsbruck, Innrain 52, A-6020 Innsbruck, Austria

* Present address: Institut für Geowissenschaften, Goethe Universität, Altenhöferallee 1, D-60438 Frankfurt a.M., Germany

Abstract

The high-pressure behavior of cordierite was investigated by means of in-situ experiments using piston-cylinder press and diamond-anvil cell. Static compression in diamond-anvil cells was conducted with various penetrating and non-penetrating pressure media (H_2O up to 2 GPa, argon and 4:1-methanol-ethanol up to 7 GPa). The measurement of lattice parameters revealed neither a significant influence on the elasticity nor any indication for effects in analogy to over-hydration within the experimental pressure ranges. Volumetric compression experiments at constant rates up

to 1.2 GPa in a piston-cylinder apparatus insinuate subtle irregularities in the low-pressure range at around ~0.35 and ~0.85 GPa. The $\Delta V/V$ contribution related to the anomalous compression behaviour in that pressure range is of the order of 5×10^{-4}. The results obtained from single-crystal X-ray diffraction between 10^{-4} and 7 GPa revealed an unexpected and anomalous linear volume decrease, corresponding to $K_{T,298}$ = 131±1 GPa for the bulk modulus and K'= -0.4±0.3 for its pressure derivative for a third-order Birch-Murnaghan equation of state. The compressional behavior of the main axis directions is anisotropic with $\beta_a^{-1} \approx \beta_b^{-1} > \beta_c^{-1}$ for an initial pressure regime up to ~3 GPa. At pressures above ~4 GPa, the compression of the *a* and *b*-axis starts to differ significantly, with the *b*-axis showing elastic softening as indicated by negative values for $\partial(\beta_b^{-1})/\partial P$. The diversification between the *a*- and *b*-axis is also expressed by the pressure-depending increase of the distortion parameter Δ. The pronounced elastic softening in both the *b*-axis and *c*-axis directions ($\partial(\beta_b^{-1})/\partial P$ = -4.3±0.9, $\partial(\beta_c^{-1})/\partial P$ = -1.2±0.8) are responsible for the apparent linear bulk compression, which indicates the structural instability and precedes a so far not reported ferroelastic phase transition to a triclinic polymorph, following a primitive lattice above the critical transition at ~6.9 GPa.

Keywords

cordierite, high pressure, compressibility, elastic softening, phase transition

Introduction

The mineral physics and structure-property relationships of the silicate mineral cordierite, corresponding to $(Mg,Fe)_2Al_4Si_5O_{18}$ in a simplified form, has received considerable attention for various outstanding physical properties. The eminent properties of cordierite include the pronounced stability at high temperatures and the remarkable robust thermal shock resistance. The ability to sustain large temperature gradients and temperature changes on a short timescale is the

consequence of relatively low thermal expansion (Hochella et al. 1979, Mirwald 1981, Ikawa et al. 1986, Camerucci et al. 2001). Another prominent aspect of the thermodynamic properties is related to the polymorphism at high temperatures (Miyashiro 1957, Langer and Schreyer 1969). The associated order/disorder phase transition, which originates from the Al,Si distribution within the alumosilicate $(Al,Si)_6O_{18}$ subunits, is accompanied by a symmetry change from orthorhombic (*Cccm*) to hexagonal (*P6/mcc*) symmetry above the critical temperature of ~1750 K (Meagher and Gibbs 1977, Putnis 1980a, Armbruster 1985a, Redfern et al. 1989, Daniels et al. 1994, Malcherek et al. 2001). Apart from the Al,Si ordering on tetrahedral sites and the mechanism of the transformation, numerous investigations focused on the structural origins of optical absorption properties, in particular on the remarkable macroscopic pleochroism in crystals. This includes the Fe^{2+},Fe^{3+} distribution (Faye et al. 1968, Goldman and Rossmann 1977, Abs-Wurmbach et al. 1989, Geiger et al. 2000a, 2000b, Khomenko et al. 2001) and, most recently, the radiocoloration and changes of the optical properties induced by irradiation (Vance and Price 1984, Nasdala et al. 2006, Weikusat et al. 2008, 2010, Miletich et al. 2010). In addition to the complex crystal chemistry, the microporous nature of the framework structure reveals the possibility for structural storage of a variable amount of extra-framework atoms (Na^+, K^+, Ca^{2+}) and molecules, such as of H_2O, CO_2, Ar or N_2 (Bulbak et al., 2002; Cohen et al. 1977, Medenbach et al. 1980, Armbruster and Bloss 1980, 1982, Armbruster 1985b, 1986, Vry et al. 1990). This provides a high flexibility of the structure for substitutions according to $^{Ch}(Na^+,K^+)_{m+n}$ $[^{[6]}((Mg,Fe^{2+},Mn^{2+})_{2-m}Li^+_m)$ $^{[4]}((Al,Fe^{3+})_{4-n}Be^{2+}_n)$ $^{[4]}Si_5O_{18}] \cdot (H_2O)_{\leq 2}$ $(CO_2)_{\leq 0.5}$ stoichiometries (Bertoldi et al., 2004).

The majority of experimental studies are devoted to property changes related to the crystal chemistry and/or variations with temperature, in particular involving high temperatures. Investigations on cordierite at high-pressure conditions originated from the need to understand thermodynamic stability conditions, but are limited to only a few individual experimental studies (Mirwald and Maresch 1980, Mirwald 1982, Mirwald et al. 1984, Koepke and Schulz 1986). Most

recently, Likhacheva et al. (2011, 2013) performed static compression on polycrystalline cordierite in aqueous media and describe a discontinuity in the volume properties in the pressure range between 4 and 5 GPa together with changes of the pressure-induced shifts of Raman modes above 4.7 GPa. Both experimental observations have been attributed to pressure-induced over-hydration by excess H_2O contents (Likhacheva et al. 2013). Potential structural changes assigned to the extra-framework channel content have also been presumed to be responsible for small volume discontinuities as observed on isothermal compression and decompression in piston-cylinder apparatus (PCA). Mirwald and Maresch (1980) and Mirwald (1982) described two discontinuities, which are supposed to occur at ~0.22 and ~0.90 GPa with a $\Delta V/V$ discontinuities of about -0.05 to -0.3 vol-% in volumetric measurements. Diffraction studies on single crystals in diamond-anvil cells later supported only the subtle discontinuity at 0.90±0.06 GPa, claiming unusual low compressibility for the pressure interval below. It is noteworthy to mention that no structural changes were observed. In addition, the possible influence of the type of pressure medium was suggested, by interaction with the structure through the open pores (Mirwald et al. 1984, Koepke and Schulz 1986). Nevertheless, the restricted number of data points, their scattering and the uncertainties of individual data points are somewhat too large with respect to the reported small volume changes, and leave some certain doubt about the significance of the existence of transitions related to structural changes. The determination of the coefficients of the elastic tensor and measurements of elastic moduli (Toohill et al. 1999, Bubeck 2009) complement the view on elasticity from static compression studies. Most recent results provide even a picture of the temperature-dependency of the elastic properties at 1 bar (Haussühl et al. 2011).

Compared to the earlier experimental investigations, both the PCA and DAC high-pressure techniques have significantly improved and, in addition, single-crystal techniques can be expected to reveal much better constraints on subtle effects. The purpose of the present study is to re-investigate the static elasticity and to compare the compressional behavior in various nominally

penetrating and non-penetrating pressure media (according to Gatta, 2008) under hydrostatic conditions. This includes compression of a large single-crystal sample in a PCA but also that of single-crystal samples in DACs. One focus of these investigations is to tackle the earlier proposed discontinuities and to extend the investigated pressure range. High-pressure structure investigations were carried out to monitor the structural evolution related to the possible interpenetration of molecular species from the pressure medium into the open framework structure. The required accuracy is achieved by employing state-of-the art single-crystal X-ray diffraction (XRD) techniques, with a sufficient density of data points across the critical pressure regions to determine high-resolution equations of states (EoSs) within the hydrostatic limits of uniform pressure conditions.

Materials and methods

Sample material and oriented crystal specimen

Single-crystal samples used in this study correspond to the sample material from Madagascar with oriented crystal specimen of homogeneous sodium-poor $Na_{0.03}[(Mg_{1.78}Fe_{0.25})Al_{3.98}Si_{4.99}O_{18})](H_2O)_{0.45}(CO_2)_{0.07}$ (sample Tsi1) and $Na_{0.03}[(Mg_{1.90}Fe_{0.12})Al_{3.99}Si_{4.98}O_{18})](H_2O)_{0.54}(CO_2)_{0.04}$ (sample Tsi2) according to Miletich et al. (2010). The Fe/(Mg+Fe) composition of individual crystal specimen was checked by energy-dispersive X-ray analyses on using a scanning-electron microscope. Crystal orientation was provided by means of polarized microscopy and conventional X-ray oscillation photographs. Double-sided polished crystal platelets, approximately 40 to 70 µm thick, were prepared from thin sections parallel (hk0)-, (001)- and (010)-plane directions (corresponding to the sample notations "Tsi1", "Tsi2_b" and "Tsi2_c"). The (hk0) section of Tsi1 approximates a crystallographic (810)-plane direction. Several cylindrically shaped flat disks (120 to 220 µm in diameter) were prepared using a microdrill device as described by Förtsch et al. (1992). For the piston-cylinder experiments a non-oriented 1.889 g cylinder (diameter: 9.60 mm;

126 height: 7.06 mm) was drilled out from a crystal specimen from Soto, Argentina (composition:
127 $Na_{0.004}[(Mg_{1.23}Fe0_{0.74}Mn_{0.05})Al_{4.02}Si_{4.95}O_{18}](H_2O)_{0.41}(CO_2)_{0.08}$, Schreyer at al. 1979; Mirwald et al.,
128 1984).

129 ***Static compression measurements in DACs***

130 All high-pressure loadings were carried out using ETH-type DAC with Be backing plates
131 and steel gaskets (stainless steel, material type 1.4310, pre-indented from initial 250 μm to the
132 starting thickness given in Table 1). Crystal specimen equilibrated in air, without additional
133 treatment prior to loading, were pressurized at room temperature using either liquid water,
134 cryogenically liquefied argon, or a water-free (4:1)-methanol-ethanol mixture acting as hydrostatic
135 pressure medium. Pressures were adjusted by means of laser-induced fluorescence following the
136 ruby scale (Mao et al. 1986). Precise pressure values were derived from the V/V_0 ratio of the unit-
137 cell volumes of quartz (Angel et al. 1997) as determined from a synthetic SiO_2 standard crystal. All
138 lattice parameters were measured with customized Huber 5042 four-circle diffractometers using
139 non-monochromatized Mo-radiation. The setting angles of diffracted Bragg peaks were recorded
140 with a point detector, using motorized slits (2 x 6 mm), employing the method of eight-position
141 diffracted-beam centering (King and Finger 1979), and using the fitting routines as implemented in
142 the SINGLE software (Angel and Finger 2011). The results of symmetry-constrained vector-least
143 squares refinements for 5 different series of individual high-pressure loadings (series A and B in
144 H_2O, series C and D in argon, series E in methanol-ethanol mix) are listed in Table 2.

145 Additional data points, in particular at pressures above the observed transition, were
146 collected on beamline ID09A at the *European Synchrotron Radiation Facility* (ESRF, Grenoble)
147 using the synchrotron X-ray beam from an undulator source. The horizontally and vertically
148 focussed beam, being monochromatized at ~30 keV (λ = 0.414384Å), gives an almost parallel
149 beam of approximately 30 × 30 μm^2 on the sample. Tiny hand-selected crystal fragments were
150 pressurized in membrane-type DACs with Boehler-Almax anvils of 0.6 mm culet size.

Measurements were performed with the DAC being mounted on a ω-rotation goniometer collecting 1°-frames in the ±30° rotation range, recording all diffraction patterns with the Mar 555 flat-panel detector (fixed 2θ=0° at a distance of 310 mm from the sample). Single-crystal sample images were finally processed with the *Crysalis* software (Agilent 2012) using more than 700 observed reflections.

Volumetric experiments with a piston-cylinder apparatus

The volumetric measurements at ambient temperature (298 K) were conducted with an electronically controlled piston-cylinder apparatus using a steel vessel with a 10 mm bore (Salzmann et al. 2006). The sample was enveloped in 2.28 g Pb-foil and accommodated inside the bore of the steel vessel. The pressure-change rate of the isothermal compression runs was 31 MPa/min. Pressure, piston displacement (pd) as a measure of volume change (ΔV) and temperature are simultaneously recorded in 0.5-second intervals during the experiment. Besides a controlling inspection of the piston displacement versus pressure loop, the data analysis mainly relies on a difference technique developed from differential pressure analysis (Mirwald and Massonne 1980, Mirwald 2005a, 2005b, 2008) where the changes in piston displacement (Δpd) per a chosen time interval (Δt: e.g. 15 s) are used as parameters (cf. Fig. 1). The difference quotient of Δpd/Δt as a parameter of the compression behavior represents a qualitative (dV/dP) compressibility coefficient. While the reading resolution of pressure is at 10^{-6} GPa due to the electronic recording technique, its relevant precision is at 5×10^{-5} GPa. The accuracy of the pressure determination is estimated to be within 50 MPa. The reading resolution of the piston displacement (Δpd), the second crucial parameter is at 10^{-5} mm, the relevant precision is 5×10^{-4} mm. Since the piston displacement measurements are of relative nature, the precision of (Δpd) allows the tracing of volume changes in the range of 5×10^{-2} mm. This corresponds to a volume change of 0.02 mm^3, thus providing a precision in ($\Delta V/V$) in the order of 10^{-4} for our 706 mm^3 cordierite sample. The low compression

and decompression rates and the use of lead as a soft pressure transmitting material keeps the friction at about 20 MPa, which implies a subordinate role in the pressure determination.

Data collection and structure refinements at 1 bar

Both sample crystals used for the high-pressure structure investigations were examined prior to loading into the pressure cell by performing a full structure refinement at ambient pressure (air) from the samples being mounted on glass fibres. X-ray intensity data collections were performed using an *Xcalibur - Oxford Diffraction* diffractometer with instrument specifications as listed in Table 3. In order to maximize data coverage and redundancy, a combination of ω and φ scans was chosen. Integrated intensities were corrected for Lorentz-polarization (Lp) and for absorption effects (analytical absorption corrections by Gaussian integration based upon the physical description of the crystal) using the CrysAlis software package (Agilent 2012). The structure refinement using anisotropic displacement parameters was performed with the SHELX-97 program (Sheldrick 1997), starting from the atomic coordinates of Miletich et al. (2010), and using neutral atomic scattering factors for Si, Al, Mg, Fe, and O from the *International Tables of Crystallography* (Wilson and Prince 1999). A full Si/Al-ordering was confirmed at the tetrahedral sites (*i.e.* $T_1$1, $T_1$6, $T_2$1, $T_2$3, $T_2$6). A mixed scattering curve of Mg and Fe was used to model the octahedral M site, but this did not lead to a significant fraction of Fe, and so the scattering curve of Mg alone was used in the last cycles of the refinement. Two extra-framework sites (here labeled as Ch1 ¼ and Ch2 ¼) as found in the difference-Fourier map were assigned using the scattering curve of oxygen as being potentially occupied by H_2O, and a further one (labeled as Na) following reported site allocations (e.g. Miletich et al. 2010). All extra-framework sites were modeled with isotropic displacement regime. Data pertaining to the XRD intensity data collection are listed in Table 3, resulting site coordinates, occupancy and displacement parameters are listed in Table 4, bond distances and other structure parameters are given in Table 5.

XRD intensity data collection at pressures < 7 GPa

An ETH-type DAC was used for all high-pressure intensity data collections using anvils with C=0.6 mm. Loading of the sample in H_2O was performed in a DAC with a low-background assembly using synthetic type-Ib single-crystal diamond backing plates (Miletich et al. 2000, 2005, Krauss et al. 2005, Periotto et al. 2011). The sample pressurized in methanol-ethanol mix, was loaded in a DAC equipped with standard Be-backing plates. Spherical standard rubies (Chervin et al. 2002) served as optical pressure sensors. The four intensity data collections of the sample in H_2O at 0.39(6), 1.41(8) and 1.75(5) GPa, including one measurement in the DAC at 1 bar without pressure medium, were performed with a *KUMA*-diffractometer using the scan settings reported in Table 3. Integrated intensity data up to $2\theta_{max}\sim70°$ were corrected for Lp and absorption effects using the ABSORB6.0 program (Angel 2004). The empirical absorption corrections for the sample crystal and the DAC components was carried out in agreement with the correction applied by Hejny et al. (2012). The seven intensity data sets of the sample in methanol-ethanol mix were collected between 10^{-4} GPa (with the crystal in the DAC without any pressure medium) and 6.98(5) GPa (Table 3). Data collections were performed with the same *Xcalibur - Oxford Diffraction* diffractometer used for the measurements at 1 bar, based on the equivalent data collection strategy, but with an exposure time of 60 s/frame. The refinements were performed with the SHELX-97 (Sheldrick 1997), starting from the structure model refined at room-*P* (with the crystal in air) and using isotropic displacement parameters. Only one channel site (*i.e.* Ch1 ¼), was successfully located for the sample in methanol-ethanol mix, while the Fourier summations yielded no significant electron densities for any channel site in the sample pressurized in H_2O (Table 4a and 4b). Site coordinates, occupancies and displacement parameters pertaining to the refinements are listed in Table 4; bond distances and other structure parameters are listed in Table 5.

Results and Discussion

Volume compression measurements in piston-cylinder pressure apparatus

Since Mirwald et al. (1984) reported a discontinuous compression behaviour at pressures below 1 GPa, we re-examined that pressure range by piston-cylinder compression experiments with the aim to provide a better volumetric resolution due to the very improved data acquisition technique. Because of the qualitative character of the volumetric technique, calibration experiments have been conducted with Pb and NaCl, both well-studied materials (Birch 1966). The continuous monitoring of compression provides (i) a good survey on the pressure characteristic of the apparatus ("apparatus function") and (ii) allows the detection of even very small changes in the compression behavior relatable to volume discontinuities or to compression anomalies of materials to be investigated.

Fig. 1 shows, as a calibration example, a compression-decompression run on Pb up to 1.5 GPa. The piston displacement (dp) versus loop (Fig. 1, top) shows the typical behaviour, i.e. in the low-pressure range up to 0.2 GPa the loop is strongly influenced by the stress-strain characteristic of the vessel plus the sample set up. The upstroke and down stroke track of Pb show a smooth course without any irregularity, apart from a slight kink on the beginning of the down stroke, which reflects the termination of the stress-strain reversal of vessel-sample set up. This situation is also reflected by the difference parameter $\Delta dp/\Delta t$ when plotted versus pressure (Fig. 1, bottom). This difference parameter is obtained by slight displacement of the pressure loop equivalent to a time interval of usually 15 seconds. This appears in the plot of piston displacement versus pressure in Fig. 1 (top) as a slightly displaced second loop. The $\Delta dp/\Delta t$ track of the calibration run on lead is very smooth. Only at low pressure and on the down stroke side of the pressure loop, the above-mentioned features related to the apparatus function are noticed. The compression-decompression results on NaCl, the second material used for calibration, are similar.

In Fig. 2 the $\Delta dp/\Delta t$ tracks (upstroke and down stroke) for the investigated cordierite sample are given. The related loop of piston displacement (dp) versus pressure loop (Fig.1, top) appears smooth. However, the inspection of the $\Delta dp/\Delta t$-tracks reveals two irregularities in the compression

250 behavior of cordierite, at 0.36 and at 0.75 GPa on compression, and at 0.75 and 0.33 GPa on
251 decompression. Instead of a smooth, slightly curved course as indicated in the plot by a curved line
252 serving as a guide to the eye, the experimental data of the compression track shows a sort of bump
253 between the two pressures, while the decompression track exhibits an almost linear behaviour in
254 that pressure interval. The two $\Delta dp/\Delta t$-discontinuities on the compression and decompression track
255 show no clear hysteresis. Since the dp versus *P* tracks show no discrete volume change, the two
256 irregularities are interpreted as a slight change in compressibility of cordierite. Based on a very
257 detailed evaluation of the compression stroke of the dp-*P*-loop, the deviations in volume were
258 calculated inferring a linear compression behavior in this pressure interval. The $\Delta V/V$ obtained is in
259 the order of 5×10^{-4}. This suggests a subtle compression irregularity, which is contained by two
260 compressibility anomalies. The implication for the overall compression behavior of cordierite is
261 small as demonstrated in Fig.3. Considering the given experimental precision, a more quantitative
262 analysis of these volumetric data is therefore limited. Nevertheless, the analytical findings re-
263 confirm in principle the occurrence of subtle irregularities in the compression behaviour in a similar
264 fashion as reported by Mirwald et al. (1984).

265 The volumetric data obtained in the PCA experiments give again evidence of this
266 phenomenon due to the fact to represent a continuous volumetric record on compression and
267 decompression. Despite all improvements of experimental techniques, including pressure
268 corrections, the data obtained here suggest subtle irregularities in the compressibility, but no evident
269 volume discontinuity. The specific volume dV/V change attributed to the anomalous compression
270 behavior between 0.35 and 0.85 GPa lies in the order of 5×10^{-4}. Considering the circumstances that
271 the PCA experiments were performed under water-free conditions, one can exclude to a certain
272 extent the influence of external fluid to control the compression behaviour of cordierite. For
273 compression at room temperature, the elastic behavior is similar to "dry" cordierite (Mirwald 1982),

and interpenetration of molecular species from the pressurizing fluids apparently requires at low pressures additional high temperatures (Le Breton and Schreyer 1993).

Equations of state and the role of pressure media

The results of high-precision XRD measurements of the lattice parameters and unit-cell volumes on static compression are summarized in Table 2. Compression data sets of single-crystal cordierite in the particular pressure media comprise various loadings of the same or equivalent sample crystals, i.e. series A and B in H_2O, and series C and D in Ar. Fig. 4 shows the evolution of the three different *P*-*V* data sets according to the (quasi)hydrostatic compression in H_2O, argon, and methanol-ethanol pressure fluids. Compression in H_2O was achieved under true hydrostatic conditions in liquid water up to 0.9 GPa, followed by quasi-hydrostatic compression in soft ice-VI up to 2.1 GPa, which represent the equilibrium phase boundary between ice-VI and ice-VII (Chen and Yoo 2011, and references therein). Data points measured above this critical pressure boundary are characterized by increasing deviatoric stress as this is manifested through significant peak broadening of XRD Bragg peak profiles. For the given quality we did not regard these measurements as relevant. Compression in argon and methanol-ethanol mix was achieved within the quasihydrostatic regime as reported by Angel et al. (2007). Nevertheless, regardless of the use of fully hydrostatically acting pressure media, the intensities of Bragg reflections significantly dropped for all samples at $P \geq 6.9$ GPa, along with drastic peak broadening, together with changes in the peak profiles, which indicate metrical changes, the existence of more than one crystal domain, and structural gradients across domain boundary walls.

Apart from a minor shift of the *P*-*V* compression data in argon due to the small difference Mg/Fe ratio of the Tsi1 and Tsi2 samples, the three *P*-*V* data sets reveal almost identical compression behavior with no visible differences for $-dV/dP$. It appears that, within the experimental error of the measurements, all samples show identical volume dependencies being

299 independent on the type of medium used for pressurization. The isothermal bulk moduli, $K_{0,298}$, for
300 compression at room temperature (298K) yield $K_{0,298}$= 137.8±1.5 GPa (in H_2O), 127.7±2.3 GPa (in
301 Ar) and 131.0±1.3 GPa (in 4:1-ME) for a parametrized fit to the *P*-*V* data sets according to a 3rd-
302 order Birch-Murnaghan EoS (Angel 2000). These results reveal almost identical compressibility
303 within the given standard deviations and considering correlation between K_0 and K' (=dK/dP) fit
304 parameters. The pressure derivatives K' result in remarkable values of -6±2, +0.4±0.9 and -0.5±0.4,
305 respectively, which corresponds to the apparent linear pressure dependency (Fig. 4). In this context,
306 the larger value for the bulk modulus in water (~138 GPa) appears to correlate with the large
307 negative value of dK/dP (-6±2), as a fit with K' set 0 yields 132.1±0.7 GPa for the bulk modulus.
308 The bulk moduli obtained here are then similar to the values of 129(1) GPa (Toohill et al. 1999) and
309 129(2) GPa (Haussühl et al. 2011), considering them to be adiabatic bulk moduli as determined
310 from Brillouin scattering and resonant ultrasound spectroscopy, respectively. In a similar fashion,
311 the discrepancy of isothermal bulk modulus K_0 being only 115(1) GPa, as reported by Likhacheva
312 et al. (2013), can be explained as a result of fitting the *P*-*V* data to a second-order Murnaghan EoS
313 with fixing K' to 4. The re-evaluation of the data up to 4 GPa fitting K_0 with setting K'=0 gives K_0 =
314 127.6 GPa for the bulk modulus, which is in perfect agreement with the results of this and earlier
315 studies (Toohill et al. 1999, Haussühl et al. 2011). Comparison of all experimental data (Fig. 4)
316 shows that, for compression at room temperature, the choice of pressurizing media is not critical.
317 This certainly applies to a water-free methanol-ethanol mixture, but also to argon in the
318 quasihydrostatic pressure regime up to 9 GPa. Using pure H_2O within the range of apparent
319 hydrostaticity (P < 2 GPa), neither the equation of state nor structure refinements give evidence for
320 a pressure-induced over-hydration. Although previous experimental studies at high *P* and *T* clearly
321 showed that Ar and H_2O can be hosted by the cordierite structure (Schreyer et al. 1960, Schreyer
322 and Yoder 1964, Armbruster 1985b), we find no evidence for interpenetration of excess Ar and
323 H_2O within the investigated pressure ranges up to 7 and 2 GPa, respectively, at room-*T*. Using pure

H_2O within the range of apparent hydrostaticity (P < 2 GPa), neither the equation of state nor structure refinements give evidence for a pressure-induced over-hydration. This might be easily understood as we remained well below the critical pressure of over-hydration (above ~4 GPa, Likhacheva et al. 2013).

The evaluation of P-V data clearly suggests an elastic anomaly obviously related to the observed structural change at ~6.9 GPa. The unusual linear compressibility is even confirmed by the compressibility data collected in H_2O with a high density of data points within a small pressure range between 10^{-4} and 2.01 GPa (Fig. 5). At first glance, the high-resolution P-V data sets, which correspond to individual measurements of the unit-cell volume with small pressure increments, do not reveal a discontinuity, neither in the volume nor for the individual axis directions. In particular, around 0.22 GPa the data suggest a smooth line with no indication for any changes in the slope (Fig. 5), i.e. neither a significant change of the bulk nor of the axial compressibilities. Plotting the calculated compressibility, i.e. as derived from ΔV and ΔP between neighbouring data points (Fig. 3), the inspection of the almost linear appearance might give hints of possible irregularities at 0.35 and at 0.85 GPa. The analysis of the unit-cell volume data suggests two to three sections, and linear fits to the volume data of the different sections yield very small differences for the slopes by ~2-3%. While the slope for the interval below 0.35 GPa is evolving in a positive fashion indicating slightly increasing stiffening, the evolution of bulk modulus for P>0.35 GPa follows a constant line, which approximates dK/dP=0. The deviation of two data points at 0.851 and 0.864 GPa (black in Fig. 3) might be considered as outliers within an applied 3σ criteria for the given errors, and hence not being significant in order to prove a change in the compressional behavior related to the previously suspected discontinuity at ~0.85 GPa.

Anisotropy of compression and of the elastic softening

348 According to the hexagonal topology of polyhedral arrangement, which follows the beryl
349 structure by ignoring the cation ordering on the T sites, the compressional anisotropy of the
350 framework structure reveals similar compression for the *a* and *b* axis, both being less compressible
351 than the *c* axis (Fig. 5). This behavior of the *c*-axis direction being comparably softer than the lattice
352 directions perpendicular to the *c*-axis has been reported for experimental investigations on beryl
353 ($\beta_{\perp}$= 1.72(4)×10^{-3} GPa^{-1} and $\beta_{//}$= 2.10(9)×10^{-3} GPa^{-1}, Hazen et al. 1986) but also for measured and
354 calculated elastic moduli in beryl (C_{11} = 306.3 GPa, C_{33} = 282.2 GPa, Yoon and Newnham 1973,
355 Prencipe et al. 2011). The behavior of similar compression of the *a*- and *b*-axis direction (Table 6)
356 corresponds rather to the expectations from symmetry aspects and is also confirmed by the linear
357 coefficients β_a=β_b= 2.4(1)×10^{-3} GPa^{-1} and β_c= 3.1(1)×10^{-3} GPa^{-1} in the pressure range below 3 GPa
358 (Likhacheva et al. 2013). Nevertheless, the similar compression in an initial stage at moderate
359 pressures starts to develop continuously into a diversification between the two axes at pressures
360 greater than 3 to 4 GPa (Fig. 6). While the *a*-axis gets the less compressible axis and shows
361 conventional stiffening with pressure (i.e. $(\partial(\beta_a^{-1})/\partial P$ = +11.2±1.3 in argon and +9.3±0.9 in 4:1
362 methanol-ethanol mix), the *b*-axis reveals anomalous behavior (i.e. $(\partial(\beta_b^{-1})/\partial P$ -4.3±0.9 and -
363 1.9±1.9) and clearly indicates to be involved in elastic softening associated with an upcoming
364 structural instability. In addition to the *b*-axis, the *c*-axis compression shows an analogous behavior
365 with getting softer as expressed by the negative value for $(\partial(\beta_c^{-1})/\partial P$ (see Table 6). The pronounced
366 anisotropy within the *ab*-plane is similar to the compressional anisotropy observed for the over-
367 hydrated cordierite above 5 GPa (Likhacheva et al. 2013), where the *a*-axis becomes the stiffest
368 (β_a= 1.6(1)×10^{-3} GPa^{-1}) in comparison to the *b*- and *c*-axis directions (β_b= 2.7(1)×10^{-3} GPa^{-1}, β_c=
369 3.0(1)×10^{-3} GPa^{-1}).

370 The diversification between the *a*- and *b*-axis is even more obvious when plotting the
371 distortion index Δ (Putnis 1980b, Selkregg and Bloss 1980). Fig. 7 shows rather constant evolutions
372 for all three individual data sets below 3 GPa, but a clear change of the trend with a positive slope

above 4 GPa, which appears to be the same within the accuracy of the data for compression in Ar and methanol-ethanol mixture. The distortion index Δ, originally a measure for the deviation from hexagonality in 2θ for selected reflections (Miyashiro 1957), was found to reach maximum values of 0.31° (Armbruster and Bloss 1980), with the value for Δ decreasing with the incorporation of Na^+, H_2O and CO_2 into the structural channels (Schreyer et al. 1979, Armbruster and Bloss 1980, Selkregg and Bloss 1980). All values, determined here from the distortion with pressure, approach the reported maximum value but lie below 0.31°.

Summarizing these findings, the compressional behavior of the main axes yields an anisotropy following the beryl structure topology with $\beta_a^{-1} \approx \beta_b^{-1} > \beta_c^{-1}$ for an initial pressure regime up to ~3 GPa. The compressional behavior of the *a*- and *b*-axis diversifies with increasing pressure and reveals increasing anisotropy of deformation within the *ab*-plane, similar to the compressional anisotropy reported for the over-hydrated cordierite (Likhacheva et al. 2013). Both the increasing anisotropy and the bulk volume compression are characterized by remarkable elastic softening effects with significantly negative $\partial(\beta^{-1})/\partial P$ coefficients, in particular obtained for the compressibilities of the *b*- and *c*-axis directions.

Structure evolution up to 7 GPa

In response to the applied pressure, the structure of cordierite reacts mainly through inter-tetrahedral tilting, with oxygen atoms acting as flexible hinges, and through the polyhedral compression of the Mg-octahedron. The evolution of the tetrahedral bond distances (Table 5) show only a subtle compression within the pressure range investigated, suggesting that the Si/Al-tetrahedra act as rigid units, whereas the inter-tetrahedral angles (*i.e.* O_26-O_23-O_21, O_21-O_26-O_23; Fig. 8, Table 5) change significantly. In particular, the angle O_21-O_26-O_23 tends to increase with *P*, whereas the angle O_26-O_23-O_21 decreases (Fig. 8, Table 5). Such mechanisms reflect the evolution of the ellipticity of the 6-membered rings of tetrahedra (6mR) perpendicular to [001]. The ellipticity ratio [here defined as $\varepsilon_{[001]} = 0.5\cdot[(O_26 \leftrightarrow O_26)+(O_21 \leftrightarrow O_21)]/[(O_23 \leftrightarrow O_23]$ is 1 for an ideal

398 undistorted ring (as expected for indialite) and a lower value indicates a higher ellipticity. Our
399 structure refinements at high pressures show that $\varepsilon_{[001]}$ is ~0.905 at ambient pressure and tends to
400 decrease with *P* (Fig. 8, Table 5), reflecting an increase on the channel ellipticity as pressure
401 increases. The increase of the ring ellipticity was postulated by Gatta and Lee (2006) and Gatta
402 (2008) as an energetically less-costly mechanism, which somewhat accommodates the effect of
403 pressure in open-framework materials. However, only a modest deformation of the [001]-channel is
404 observed within the *P*-range investigated (Fig. 8). While the data scatter in the low-*P* range does not
405 reflect any clear deviation from linear trends, individual quantities (see Fig. 7 and 8) of the
406 structures above 6 GPa might be interpreted as a precursor effect for the transformation at 6.9 GPa.
407 The high-pressure structure refinements show a significant compression of the Mg-
408 polyhedron, as shown in Fig. 9, Table 5. The compressibility coefficient of the Mg-polyhedron,
409 here derived by linear regression through the data points, is $\beta_{poly}(MgO_6) = 1.0(1) \times 10^{-2}$ GPa^{-1},
410 which leads to a polyhedral modulus of $K_{poly}(MgO_6) = 100(9)$ GPa. It is remarkable to point out that
411 the Mg-polyhedron is, at a significant level, not deformed in response to the applied pressure, as
412 shown by the evolution of the polyhedron distortion coefficient with *P* (ξ in Table 5). This
413 someway reflects the hexagonal topology of the cordierite framework, which controls the almost
414 isotropic compression of the Mg-polyhedron.
415 The structure investigation under increasing H_2O pressure was mainly aimed to elucidate
416 any potential pressure-induced over-hydration in cordierite, such as recently reported by
417 Likhacheva et al. (2013). A careful inspection of the difference-Fourier maps of the electron density
418 of the H*P*-refinements did not give any evidence for a pressure-driven penetration of molecules of
419 the *P*-medium through the [001] channel, as previously observed in other classes of open-
420 framework materials compressed in hydrous media (Gatta 2008, 2010). In response to the modest
421 applied $P(H_2O)$ in this experiment ($P < 2$ GPa), as limited by the quasihydrostaticity of ice-VI
422 before transforming to ice-VII at 2.1 GPa, the structure of cordierite does not show any significant

deformation mechanism. The ellipticity ratio of the 6mR running along [001] is constant within the *e.s.d.*, and even the softest unit of the cordierite structure, represented by the Mg-octahedron, appears to be only marginally compressed. The structure refinements clearly suggest no pressure-induced changes related to the possible re-arrangement of H_2O molecules on extra-framework sites, which would have been indicative for over-hydration effects.

Changes of lattice metrics above 7 GPa

Any attempt to increase the pressure to values above ~7.0 GPa resulted in difficulties to center XRD peak profiles, which show significant broadening and did not allow to obtain any reliable high-precision data points for equation of state measurements. The optical inspection of the pressurized sample indicated inhomogeneities, the formation of domains, and optically visible strain across the sample crystals (Fig. 10). Using the strongest reflections of such a multi-domain crystal, the refinement of unit-cell parameters clearly indicated small but significant deviations from 90° of orthorhombic α, β and γ angles. In order to overcome emerging strain in rather large crystals, tiny micrometer-sized sample crystals were chosen for investigations using synchrotron radiation. The sample loading of small crystal fragments provided almost unstrained single-domain crystals above the transition. The determined unit cell proves the orthorhombic-to-triclinic transition with consistent deviations from orthogonal lattice settings, in particular with the β angle around ~86.0° and the γ angle at 89.0° for base-vector settings corresponding to the orthorhombic *C*-centered unit cell at low pressures (Table 2). The lattice distortion appears to occur in a similar fashion such as reported for beryl, where the hexagonal structure undergoes a transition to a structure of triclinic symmetry above ~14 GPa (Prencipe et al. 2011). The unit-cell volume of cordierite here reveals a clear discontinuity across the critical transition pressure showing a spontaneous $\Delta V/V$ of approximately -6.9% as determined from unit-cell volumes measured at 7.53 and 9.0 GPa. The appearance of such a significant volume discontinuity associated with the transformation clearly suggests the structural transition to be first order in character. In this context, the pronounced

anomaly of the compression behaviour can be understood as elastic softening phenomenon typically associated with first-order transitions. The changes at the individual crystallographic axes follow the anisotropy observed for the compression of the orthorhombic polymorph. It is remarkable that the evolving anisotropy, as expressed by the different behavior between the *a*- and *b*-axis directions, leaves its trace even across the transition. A comparably large spontaneous shortening along the *a*-axis direction from ~98.5 % to ~91.0 % of the original value is the most striking change associated with observed structural transformation. Any attempt to refine a triclinic structure model from the collected XRD intensity data sets did not yield yet a satisfying structure refinement of appropriate quality and will be reported elsewhere.

Implications

The experimental findings of this study allow improving the knowledge on the phase-stability and elastic behaviour of cordierite. Up to date, the phase-diagram of cordierite was characterised by only two distinct fields, associated to Al,Si-order/disorder phase transition with a low-*T* orthorhombic phase (*Cccm,* at $T<1750$ K, $P=0.0001$ GPa) and a high-*T* hexagonal phase (*P*6/*mcc*, at $T>1750$ K, $P=0.0001$ GPa) (Miyashiro 1957, Langer and Schreyer 1969, Meagher and Gibbs 1977, Putnis 1980a, Armbruster 1985a, Redfern et al. 1989, Daniels et al. 1994, Malcherek et al. 2001). Our results lead to an enrichment of the phase-diagram with a new high-*P* triclinic polymorph at $P>7$ GPa and $T=293$ K. The orthorhombic-to-triclinic phase transition is governed by a volume contraction of about 7%. We still do not know the effect of temperature on the transition pressure, which will be investigated in the near future. In addition, the anomalous compressional pattern of the orthorhombic cordierite (with a negative bulk modulus *P*-derivative) has now a realistic explanation: it appears to be governed by the orthorhombic-to-triclinic transition. The results of this study are expected to improve the modelling of phase equilibria of petrological interest, as cordierite is a common mineral in medium and high-grade pelitic metamorphic rocks or as

porphyroblasts in hornfels found in contact metamorphic zones. Even in material sciences, where cordierite has received considerable attention for its pronounced stability at high temperatures, low thermal expansion and an uncommon robust thermal shock resistance (Hochella et al. 1979, Mirwald 1981, Ikawa et al. 1986, Camerucci et al. 2001), our high-quality elastic data of the low-*P* polymorph and the *P*-induced densification in response to the orthorhombic-to-triclinic phase-transition would open a new scenario with further potential applications of this ceramic material.

Acknowledgments

We thank Olaf Medenbach (Bochum) for the providing us crystal disks suitable for DACs, Herta Effenberger (Vienna) for performing the oscillation film photographs, Ilona Fin (Heidelberg) and Andreas Wagner (Vienna) for the sample preparation, Ilse Glass (Heidelberg) for EDX analyses, and Angela Ullrich, Pascal Schouwink and Thomas Pippinger for their assistance in collecting individual EoS data points at Heidelberg. We would like to thank Michael Hanfland (ESRF Grenoble) for his generous support on beamline ID09A. R.M. wants to express his gratitude to the Laboratorium für Kristallographie, ETH Zürich, to have facilitated the use of equipment in the former high-pressure X-ray crystallography lab for the compressibility measurements in H_2O. T.L. ist grateful to the European Research Council (ERC Starting Grant SULIWA) and the Austrian Science Fund (START award Y391) for financial support. Finally we thank Anna Likhacheva, Alexandra Friedrich and one anonymous referee for their valuable suggestions, which significantly improved the manuscript.

References

Abs-Wurmbach, I., Boberski, C., and Hafner, S. (1989) Zum Problem des Einbaus von dreiwertigem Eisen in den Cordierit: Synthesen und Mößbauerspektroskopie. Fortschritte Mineralogie, 66, 1

Agilent (2012) Crysalis Pro: User Manual. Agilent Technologies, Yarnton

Angel, R.J., Allan, D.R., Miletich, R., and Finger, L.W. (1997) The use of quartz as an internal pressure standard in high pressure crystallography. Journal of Applied Crystallography, 30, 461-466.

Angel, R.J. (2004) Absorption corrections for diamond-anvil pressure cells implemented in a software package Absorb-6.0. Journal of Applied Crystallography, 37, 486-492

Angel, R.J., Bujak, M., Zhao, J., Gatta, G.D. and Jacobsen, S.J. (2007) Effective hydrostatic limits of pressure media for high-pressure crystallographic studies. Journal of Applied Crystallography, 40, 26-32.

Angel, R.J. (2000) Equations of state. In: R.M. Hazen and R.T. Downs (Eds.) High-temperature and high-pressure crystal chemistry, Reviews in Mineralogy and Geochemistry, 41, 35-60.

Angel, R.J. and Finger, L.W. (2011) Single: a program to control single-crystal diffractometers. Journal of Applied Crystallography, 44, 247-251

Armbruster, T. (1985a) Crystal structure refinement, Si,Al-ordering, and twinning in "pseudo-hexagonal" Mg-cordierite. Neues Jahrbuch Mineralogie, Monatshefte, 1985, 255-267

Armbruster, T. (1985b) Ar, N_2, and CO_2 in the structural cavities of cordierite, and optical and X-ray single-crystal study. Physics and Chemistry of Minerals, 12, 233-245

Armbruster, T. (1986) Role of Na in the structure of low-cordierite: A single-crystal X-ray study. American Mineralogist, 71, 746-757

Armbruster, T., and Bloss, F.D. (1980) Channel CO_2 in cordierite. Nature, 286, 140-141

Armbruster, T., and Bloss, F.D. (1982) Orientation and effects of channel H_2O and CO_2 in cordierite. American Mineralogist, 67, 284-291

Balic-Zunic, T., and Vickovic, I. (1996) *IVTON* - a program for the calculation of geometrical aspects of crystal structures and some crystal chemical applications. Journal of Applied Crystallography, 29, 305-306

523 Bertoldi, C., Proyer, A., Garbe-Schönberg, D., Behrens, H., and Dachs, E. (2004) Comprehensive
524 chemical analyses of natural cordierites: implications for exchange mechanisms. Lithos, 78, 389-
525 409
526 Birch, F. (1966) Compressibility, elastic constants. In Clark, S.P., Handbook of physical constants.
527 Geological Society of America, Memoir 97, 97-173.
528 Bubeck, C. (2009) Direction dependent mechanical properties of extruded cordierite honey-combs.
529 Journal of European Ceramical Society, 29, 3113-3119
530 Bulbak, T.A., Shvedenkov, G.Y., Lepezin, G.G. (2002) On saturation of magnesian cordierite with
531 alkanes at high temperatures and pressures. Physics and Chemistry of Minerals, 116, 140-154
532 Camerucci, M.A., Urretavizcaya, G., and Cavalieri, A.L. (2001) Mechanical behaviour of cordierite
533 and cordierite-mullite materials evaluated by indentation techniques. Journal of European
534 Ceramic Society, 21, 1195-1204
535 Chen, J.Y., and Yoo, C.S. (2011) High density amorphous ice at room temperature. Proceedings of
536 the National Academy of Sciences, 108, 19, 7685-7688
537 Chervin, J.C., Canny, B. and Mancinelli, M (2002) Ruby-spheres as pressure gauge for optically
538 transparent high pressure cells. High Pressure Research, 21, 305-314
539 Cohen, J., Ross, F., and Gibbs, G.V. (1977) An X-ray and neutron diffraction study of hydrous low
540 cordierite. American Mineralogist, 62, 67-78
541 Daniels, P., Wunder, B., Sahl K., and Schreyer, W. (1994) Changing lattice metrics of synthetic
542 cordierites: the metastable hexagonal to orthorhombic transformation sequence during isothermal
543 annealing. European Journal of Mineralogy, 6, 323-335
544 Faye, G.H., Manning, P.G., and Nickel, E.H. (1968) The polarized optical absorption spectra of
545 tourmaline, cordierite, chloritoid and vivianite: ferric-ferrous electron interaction aqs a source of
546 pleochroism. American Mineralogist, 53, 1174-1201

Förtsch, E., Uhr, W., and Wondratschek, H. (1992) A novel application of the spindle stage. Microscope 40, 31-36

Gatta, G.D. (2008) Does porous mean soft? On the elastic behaviour and structural evolution of zeolites under pressure. Zeitschrift für Kristallographie, 223, 160–170.

Gatta G.D. (2010) Microporous materials at high pressure: Are they really soft? *In*: E. Boldyreva and P. Dera (eds.), *High-Pressure Crystallography: From Fundamental Phenomena to Technological Applications*, NATO Science for Peace and Security – Series B (Physics and Biophysics), p. 481-491, Springer Science, ISBN 978-90-481--9257-1 (doi:10.1007/978-90-481-9258-8_39).

Gatta, G.D. and Lee, Y. (2006) On the elastic behavior of zeolite mordenite. A synchotron powder diffraction study. Physics and Chemistry of Minerals, 32, 726–732.

Geiger, C.A., Rager, H., and Czank, M. (2000a) Cordierite: III. the site occupation and concentration of Fe^{3+}. Contributions in Mineralogy and Petrology, 140, 344-352

Geiger, C.A., Armbruster, T., Khomenko, V., and Quartieri, S. (2000b) Cordierite: I. The coordination of Fe^{2+}. American Mineralogist, 85, 1255-1264

Goldman, D.S., and Rossmann, G.R. (1977) Channel constituents in cordierite. American Mineralogist, 62, 1144-1157

Haussühl, E., Vinograd, V.L., Krenzel, T.F., Schreuer, J., Wilson, D.J., and Ottinger, J, (2011) High temperature elastic properties of Mg-cordierite: Experimental studies and atomistic simulations. Zeitschrift für Kristallographie, 226, 236-253

Hazen, R.M., Au, A.Y., and Finger, L.W. (1986) High pressure crystal chemistry of beryl ($Be_3Al_2Si_6O_{18}$) and euclase ($BeAlSiO_4OH$). American Mineralogist, 71, 977-984

Hejny, C., Miletich, R., Jasser, A., Schouwink, P., Crichton, W., and Kahlenberg, V. (2012) Second order $P\bar{6}c2$-P31c structural transition and structural crystallography of the cyclosilicate benitoite, $BaTiSi_3O_9$, at high pressure. American Mineralogist, 97, 1747-1763

572 Hochella, M., Brown, G., Ross, F., and Gibbs, G. (1979) High temperature crystal chemistry of
573 hydrous Mg- and Fe-cordierites. American Mineralogist, 64, 337–351.
574 Ikawa, H., Otagiri, T., Imai, O., Suzuki, M., Urabe, K., and Udagawa, S. (1986) Crystal structures
575 and mechanism of thermal expansion of high cordierite and its solid solutions. Journal of the
576 American Ceramic Society, 69, 492-498
577 Khomenko, V.M., Langer, K., and Geiger, C.A. (2001) Structural locations of the iron ions in
578 cordierite: a spectroscopic study. Contributions in Mineralogy and Petrology, 141, 381-396
579 King, H.E., and Finger, L.W. (1979) Diffracted beam crystal centering and its application to high-
580 pressure crystallography. Journal of Applied Crystallography, 12, 374-378
581 Krauss, G., Reifler, H., and Steurer, W. (2005) Conically shaped single-crystalline diamond
582 backing plates for a diamond anvil cell. Review in Scientific Instruments, 76, 105104, 1-5
583 Koepke, J., and Schulz, H. (1986) Single crystal structure investigation under high pressure of the
584 mineral cordierite with an improved high-pressure cell. Physics and Chemistry of Minerals, 13,
585 165-173
586 Langer, K., and Schreyer, W. (1969) Infrared and powder X-ray diffraction studies of the
587 polymorphism of cordierite. American Mineralogist, 54, 1442-1459
588 Le Breton, N. and Schreyer, W. (1993) Experimental CO_2 incorporation into Mg-cordierite:
589 nonlinear behaviour of the system. European Journal of Mineralogy, 5, 427-438
590 Likhacheva, A.Yu, Goryainov, S.V., Krylov, A.S., Bul'bak, T.A., and Prasad, P.S.R. (2011) Raman
591 spectroscopy of natural cordierite at high water pressure up to 5 GPa. Journal of Raman
592 spectroscopy, 43, 559-563
593 Likhacheva, A.Yu, Goryainov, S.V., and Bul'bak, T.A., (2013) An X-ray diffraction study of the
594 pressure-induced hydration in cordierite at 4-5 GPa. American Mineralogist, 98, 181-186
595 Makovicky, E., and Balic-Zunic, T. (1998) New Measure of Distortion for Coordination Polyhedra.
596 Acta Crystallographica B, 54, 766-773

Malcherek, T., Domeneghetti, M.C., Tazzoli, V., Ottolini, L., McCammon, C., and Carpenter, M.A. (2001) Structural properties of ferromagnesian cordierites. American Mineralogist, 86, 66-79

Mao, H.K., Xu, J., and Bell, P.M. (1986) Calibration of the ruby pressure scale to 800 kbars under quasihydrostatic conditions. Journal of Geophysical Research, 9, 4673-4676

Meagher, E.P., and Gibbs, G.V. (1977) The polymorphism of cordierite: II. The crystal structure of indialite. Canadian Mineralogist, 15, 43-49

Medenbach, O., Maresch, W.V., Mirwald, P.W., and Schreyer, W. (1980) Variation of refractive index of synthetic Mg-cordierite with H_2O content. American Mineralogist, 65, 367-373

Miletich, R., Reifler, H., and Kunz, M. (1999): The "ETH diamond-anvil cell" design for single-crystal XRD at non-ambient conditions. Acta Crystallographica, A55: Abstr. P08.CC.001

Miletich, R., Allan, D.R., and Kuhs, W.F. (2000) High-pressure single-crystal techniques. In R.M. Hazen (ed.) "High-Temperature and High-Pressure Crystal Chemistry", MSA Reviews in Mineralogy and Geochemistry, 41, 445-520

Miletich, R., Hejny, C., Krauss, G., and Ullrich, A. (2005) Diffraction techniques: Shedding light on structural changes. In R. Miletich (ed.) Mineral Behaviour at Extreme Conditions, EMU Notes, Volume 7, Eötvös University Press, pp 281-338

Miletich, R., Gatta, G.D., Redhammer, G.J., Burchard, M., Meyer, H.P., Weikusat, C., Rotiroti, N. Glasmacher, U.A., Trautmann, C. and Neumann, R. (2010) Structure alterations in microporous $(Mg,Fe)_2Al_4Si_5O_{18}$ crystals induced by energetic heavy-ion irradiation. Journal of Solid State Chemistry, 183, 2372–2381.

Mirwald, P.W., and Massonne, H.J. (1980) The low-high quartz and quartz-coesite transition to 40 Kbars between 600 and 1600°C and some reconnaissance data on the effect of $NaAlO_2$ component on the low quartz-coesite transition. Journal of Geophysical Research, B85, 6983-6990.

Mirwald, P.W., and Maresch, W.V. (1980) Ein Hochdruckphasenübergang in Cordierit. Naturwissenschaften, 67, 253-254

Mirwald, P.W. (1981) Thermal expansion of anhydrous Mg-cordierite between 25 and 900°C. Physics and Chemistry of Minerals, 7, 268-270

Mirwald, P.W. (1982) A high-pressure phase transition in cordierite. American Mineralogist, 67, 277-283

Mirwald, P.W., Malinowski, M., and Schulz, H. (1984) Isothermal compression of low-cordierite to 30 Kbar (25° C). Physics and Chemistry of Minerals, 11, 140-148.

Mirwald, P.W. (2005a) The fine-structure of the dehydration boundary of brucite ($Mg(OH)_2$ up to 2.5 GPa – Indications of not-smooth PVT behaviour of supercritical H_2O. European Journal of Mineralogy, 17, 537-542.

Mirwald, P.W. (2005b) Evidence of anomaly boundaries of water at high pressure from compression and $NaCl*2H_2O$ dehydration experiments. Journal of Chemical Physics 123, 124715, 1-6.

Mirwald, P.W (2008) Experimental study of the dehydration reactions gypsum-bassanite and bassanite-anhydrite at high pressure: Indication of anomalous behaviour of H_2O at high pressure in the temperature range of 50-300 °C. Journal of Chemical Physics, 128, 074502, 1-7.

Miyashiro, A. (1957) Cordierite-indialite relations. American Journal of Science, 255, 43-62

Nasdala, L., Wildner, M., Wirth, R., Groschopf, N., Pal, D.C., and Möller, A. (2006): Alpha particle haloes in chlorite and cordierite. Mineralogy and Petrology, 86, 1-27

Periotto, B., Nestola, F., Balic-Zunic, T., Angel, R.J., Miletich, R., and Olsen, L.A. (2011) Comparison between beryllium and diamond backing plates diamond anvil cells: Application to single-crystal X-ray diffraction high-pressure data. Review in Scientific Instruments, 82, 055111, 1-5

Prencipe, M., Scanavino, I., Nestola, F., Merlini, M., Civalleri, B., Bruno, M., and Dovesi, R. (2011) High-pressure thermo-elastic properties of beryl ($Al_4Be_6Si_{12}O_{36}$) from ab initio calculations, and observations about the source of thermal expansion. Physics and Chemistry of Minerals, 38, 223-239

Putnis, A. (1980a) Order-modulated structures and the thermodynamics of cordierite reactions. Nature, 287, 128-131

Putnis, A. (1980b) The distortion index in anhydrous Mg cordierite. Contributions in Mineralogy and Petrology, 74, 135-141

Redfern, S.A.T., Salje, E.K.H., Maresch, W., and Schreyer, W. (1989) X-ray powder diffraction and infrared study of the hexagonal to orthorhombic phase transition in K-bearing cordierite. American Mineralogist, 74, 1293-1299

Salzmann, C., Loerting, Th., Klotz, S., Mirwald, P.W., Hallbrucker, A, and Mayer, E. (2006) Isobaric annealing of high-density amorphous ice between 0.3 and 1.9 GPa: in situ values and structural changes. Physical Chemistry Chemical Physics, 8, 386-397.

Schreyer, W., Gordillo, and C.E., Werding, G. (1979) A new sodian-beryllian cordierite from Soto, Argentina, and the relationship between distorsion index, Be content, and state of hydration. Contributions Mineralogy Petrology 70, 421-428.

Schreyer, W., Yoder, H.S.Jr., and Aldrich, L.T. (1960) Synthesis of argon-containing cordierite. Annual Report of the Geophysical Laboratory, 1959-1960, Carnegie Institute of Washington Year Book, 59, 94-96

Schreyer, W., and Yoder, H.S.Jr. (1964) The system Mg-cordierite-H_2O and related rocks. Neues Jahrbuch für Mineralogie, Abhandlungen, 101, 271-342

Selkregg, K.R., and Bloss, F.D. (1980) Cordierites: compositional controls of Δ, cell parameters, and optical properties. American Mineralogist, 65, 522-533

669 Sheldrick, G.M. (1997) SHELXS-97. Program for the Solution of Crystal Structures. University of
670 Göttingen, Germany 1997.
671 Toohill, K., Siegesmund, S., and Bass J.D. (1999) Sound velocities and elasticity of cordierite and
672 implications for deep crustal seismic anisotropy. Physics and Chemitry of Minerals, 26, 333-343
673 Vance, E.R., and Price, D.C. (1984) Heating and radiation effects on the optical and Mössbauer
674 spectra of Fe-bearing cordierites. Physics and Chemistry of Minerals, 10, 200-208
675 Vry, J.K., Brown, P., and Valley, J. (1990) Cordierite volatile content and the role of CO_2 in high-
676 grade metamorphism. American Mineralogist, 75, 71-88
677 Weikusat, C., Glasmacher, U.A., Miletich, R., Neumann, R., and Trautmann, C. (2008) Raman
678 spectroscopy of heavy ion induced damage in cordierite. Nuclear Instruments and Methods in
679 Physical Research B, 266, 2990-2993
680 Weikusat, C, Miletich R., Glasmacher, U.A., Trautmann, C., and Neumann, R. (2010) Heavy ion
681 irradiation on crystallographically oriented cordierite and the conversion of molecular CO_2 to
682 CO - A Raman spectroscopic study. Physics and Chemistry of Minerals, 37, 417-424
683 Wilson, A.J.C., and Prince, E. (1999) International Tables for Crystallography, Volume C,
684 Mathematical, physical and chemical tables (third edition), 578 p., Kluwer, Dordrecht.
685 Yoon, H.S., and Newnham, R.E. (1973) The elastic properties of beryl. Acta Crystallographica
686 A29, 507-509

Table 1. Details of the high-pressure DAC loadings (pressure range, pressure-chamber dimensions) and of the individual crystal specimen (crystal material, orientation, dimensions).

HP-measurement	DAC type/ backing plates/ anvils‡	*P* range (GPa)	crystal	orientation	dimensions (μm)	pressure chamber (μm)
EoS in H_2O (series A)	ETH/ polyBe/ sbc, C=0.6mm	0.07-0.21	Tsi1#1	disk //(hk0)	∅ = 155, H = 45	∅ = 230, H = 75
EoS in H_2O (series B)	ETH/ polyBe/ sbc, C=0.6mm	0.06-2.01	Tsi1#1*	disk //(hk0)	∅ = 155, H = 45	∅ = 235, H = 85
EoS in Ar (series C)	ETH/ polyBe/ sbc, C=0.6mm	1.28-6.44	Tsi2_b#1	plate //(010)	210 × 100 × 65	∅ = 250, H = 115
EoS in Ar (series D)	ETH/ polyBe/ sbc, C=0.6 mm	0.89-4.67	Tsi2_b#2	plate //(010)	165 × 80 × 65	∅ = 250, H = 95
EoS in M-E (series E)	ETH/ polyBe/ sbc, C=0.6 mm	1.05-6.61	Tsi1#1*	disk //(hk0)	∅ = 155, H = 45	∅ = 250, H = 105
$P>P_c$ (series F and G)	mDAC/ --- / BA, C=0.6mm	> 7.0	Tsi2_c**	plate //(001)	30 × 30 × 10	∅ = 250, H = 80
Structure in H_2O	ETH/ diaBP/ sbc, C=0.6 mm	0.39-1.75	Tsi2_b#3	plate //(010)	160 × 140 × 60	∅ = 300, H = 120
Structure in M-E	ETH/ polyBe/ sbc, C=0.6 mm	1.07-6.98	Tsi1#2	disk //(hk0)	∅ = 195, H = 50	∅ = 300, H = 120

‡ Abbreviations: "ETH" = ETH diamond-anvil cell, "mDAC" = membrane-type diamond-anvil cell, "polyBe" = polycrystalline beryllium backing plate, "diaBP" = Sumicrystal UP7020 diamond backing plate, "sbc" = standard brilliant-cut diamond anvil, "BA" = Böhler-Almax diamond anvil, "C" = unbevelled culet-face diameter

* same crystal as used for series A ** several micro-size crystal fragments from Tsi2_c used for synchrotron XRD

Table 2. Lattice parameters, unit-cell volumes and calculated distortion parameter Δ of cordierite in air and at pressurized in water, argon and 4:1 methanol-ethanol mixture.

no.	*V*-Qz (Å^3)	*P* (GPa)	*a* (Å)	*b* (Å)	*c* (Å)	*V* (Å^3)	Δ (°)
cordierite in air							
A00‡	---	0.0001	17.0719(4)	9.7224(3)	9.3489(2)	1551.74(6)	0.2540
B00‡	---	0.0001	17.0721(8)	9.7211(8)	9.3496(8)	1551.66(14)	0.2567
C00‡	---	0.0001	17.0738(8)	9.7193(8)	9.3451(8)	1550.78(15)	0.2619
cordierite in water							
B43*[1]	113.048(16)	0.0001	17.0717(9)	9.7230(6)	9.3493(6)	1551.87(16)	0.2527
B16	112.888(33)	0.060(16)	17.0710(6)	9.7239(4)	9.3457(4)	1551.35(9)	0.2502
A02	112.874(19)	0.065(14)	17.0710(6)	9.7233(4)	9.3462(3)	1551.34(9)	0.2513
B04	112.872(20)	0.066(10)	17.0715(6)	9.7232(5)	9.3457(4)	1551.29(10)	0.2521
B03	112.868(20)	0.067(10)	17.0715(5)	9.7233(4)	9.3457(3)	1551.30(8)	0.2519
B07	112.770(20)	0.100(10)	17.0701(6)	9.7222(4)	9.3448(3)	1550.85(9)	0.2524
B05	112.753(23)	0.105(12)	17.0694(5)	9.7227(3)	9.3449(3)	1550.89(8)	0.2507
B08	112.709(33)	0.120(16)	17.0688(5)	9.7215(3)	9.3445(3)	1550.58(7)	0.2523
A03	112.650(22)	0.140(11)	17.0680(5)	9.7212(4)	9.3439(3)	1550.35(8)	0.2520
B06	112.592(31)	0.160(15)	17.0671(5)	9.7211(4)	9.3432(3)	1550.15(9)	0.2512
B02	112.499(23)	0.191(11)	17.0667(5)	9.7214(3)	9.3419(3)	1549.94(8)	0.2502
B17	112.499(22)	0.191(11)	17.0668(6)	9.7204(4)	9.3423(4)	1549.85(10)	0.2522
B01	112.475(22)	0.199(11)	17.0659(7)	9.7204(5)	9.3421(4)	1549.74(10)	0.2513
A01	112.448(19)	0.209(9)	17.0661(5)	9.7202(3)	9.3420(3)	1549.70(7)	0.2519
B10	112.421(41)	0.218(20)	17.0656(5)	9.7199(4)	9.3415(3)	1549.53(8)	0.2519
B15	112.417(27)	0.219(13)	17.0647(7)	9.7195(5)	9.3417(4)	1549.42(11)	0.2517
B18	112.380(22)	0.232(11)	17.0646(5)	9.7188(4)	9.3418(3)	1549.31(8)	0.2528
B09	112.376(22)	0.233(11)	17.0638(5)	9.7188(4)	9.3415(3)	1549.19(8)	0.2520
B14	112.336(27)	0.247(13)	17.0641(3)	9.7186(3)	9.3414(3)	1549.17(8)	0.2527
B13	112.296(27)	0.261(13)	17.0631(5)	9.7188(4)	9.3402(3)	1548.91(8)	0.2512
B12	112.227(24)	0.284(12)	17.0621(5)	9.7176(4)	9.3395(3)	1548.51(8)	0.2524
B11	112.087(32)	0.333(16)	17.0602(5)	9.7167(4)	9.3385(3)	1548.04(8)	0.2520
B19	111.931(26)	0.388(13)	17.0600(7)	9.7166(5)	9.3376(4)	1547.84(11)	0.2520
B20	111.640(27)	0.491(13)	17.0543(5)	9.7135(3)	9.3339(3)	1546.22(8)	0.2516
B22	111.590(44)	0.509(22)	17.0535(14)	9.7130(9)	9.3339(8)	1546.08(23)	0.2517
B23	111.432(20)	0.566(10)	17.0523(6)	9.7119(4)	9.3316(4)	1545.42(10)	0.2525
B24	111.268(27)	0.626(13)	17.0491(6)	9.7101(4)	9.3302(3)	1544.60(9)	0.2524
B25	111.051(22)	0.706(11)	17.0462(5)	9.7088(5)	9.3279(4)	1543.75(10)	0.2517
B21	111.004(26)	0.724(13)	17.0450(6)	9.7084(4)	9.3273(3)	1543.48(9)	0.2511
B26	110.667(15)	0.851(8)	17.0426(7)	9.7062(5)	9.3239(4)	1542.35(10)	0.2526
B28	110.632(20)	0.864(10)	17.0415(7)	9.7059(5)	9.3228(4)	1542.01(11)	0.2520
B29	110.587(48)	0.881(24)	17.0379(6)	9.7044(4)	9.3231(3)	1541.52(8)	0.2509
B30	110.476(25)	0.924(12)	17.0377(5)	9.7035(4)	9.3217(3)	1541.11(9)	0.2524
B27	110.443(33)	0.937(17)	17.0363(6)	9.7034(4)	9.3211(3)	1540.88(9)	0.2511

B31	110.150(27)	1.051(13)	17.0330(5)	9.7010(3)	9.3178(3)	1539.64(7)	0.2520
B32	109.975(17)	1.120(8)	17.0295(6)	9.6990(4)	9.3160(3)	1538.71(9)	0.2520
B33	109.896(17)	1.150(8)	17.0282(5)	9.6988(3)	9.3150(3)	1538.40(7)	0.2509
B34	109.744(14)	1.212(7)	17.0266(5)	9.6970(4)	9.3139(3)	1537.78(8)	0.2526
B35	109.641(17)	1.254(8)	17.0240(5)	9.6960(3)	9.3125(3)	1537.15(7)	0.2517
B36	109.325(12)	1.383(6)	17.0204(5)	9.6939(4)	9.3090(3)	1535.93(8)	0.2517
B37	109.108(20)	1.473(10)	17.0160(6)	9.6914(4)	9.3061(4)	1534.66(9)	0.2516
B38	108.814(19)	1.598(9)	17.0112(8)	9.6886(5)	9.3029(5)	1533.24(12)	0.2517
B39	108.645(17)	1.670(8)	17.0076(6)	9.6863(4)	9.3002(3)	1532.12(9)	0.2521
B40	108.435(19)	1.761(9)	17.0055(10)	9.6854(6)	9.2976(6)	1531.36(15)	0.2515
B41	108.149(22)	1.887(11)	17.0002(7)	9.6823(5)	9.2943(4)	1529.84(11)	0.2516
B42	107.863(40)	2.013(20)	16.9955(10)	9.6800(6)	9.2915(6)	1528.60(16)	0.2508
cordierite in argon							
D05*[2]	---	0.0001	17.0727(5)	9.7200(4)	9.3436(4)	1550.54(10)	0.2594
D01	110.546(25)	0.889(12)	17.0318(6)	9.7006(13)	9.3188(8)	1539.64(25)	0.2515
C01	109.502(22)	1.275(9)	17.0123(8)	9.6877(17)	9.3085(8)	1534.13(31)	0.2546
C02	108.123(38)	1.860(17)	16.9886(7)	9.6769(18)	9.2923(9)	1527.62(32)	0.2491
D02	107.432(18)	2.212(9)	16.9773(6)	9.6699(11)	9.2833(7)	1524.02(22)	0.2500
D03	105.216(25)	3.330(12)	16.9344(7)	9.6436(11)	9.2559(7)	1511.58(23)	0.2529
C03	104.496(25)	3.658(14)	16.9201(6)	9.6343(14)	9.2421(7)	1506.58(26)	0.2549
C04	103.729(19)	4.092(11)	16.9073(10)	9.6276(21)	9.2324(11)	1502.83(38)	0.2536
D04	102.923(28)	4.674(14)	16.8846(8)	9.6088(11)	9.2146(7)	1494.99(24)	0.2644
C05	101.267(32)	5.630(22)	16.8538(10)	9.5821(22)	9.1872(10)	1483.69(39)	0.2813
C06	100.107(45)	6.439(32)	16.8277(15)	9.5597(36)	9.1633(16)	1474.08(61)	0.2952
cordierite in 4:1 methanol-ethanol mix							
E09*[3]	112.994(12)	0.0001	17.0716(7)	9.7234(10)	9.3494(6)	1551.94(17)	0.2518
G00	---	0.0001	17.0930(6)	9.7289(4)	9.347(5)	1554.4(8)	0.2648
E01	110.071(16)	1.052(6)	17.0246(6)	9.7008(11)	9.3224(6)	1539.61(20)	0.2432
E08	109.081(15)	1.454(6)	17.0087(5)	9.6912(8)	9.3111(7)	1534.79(15)	0.2440
E02	108.242(19)	1.813(9)	16.9933(6)	9.6835(9)	9.3010(6)	1530.53(18)	0.2418
E07	105.646(17)	3.050(8)	16.9441(7)	9.6536(14)	9.2686(7)	1516.08(23)	0.2446
E03	103.909(18)	3.994(9)	16.9081(7)	9.6234(10)	9.2473(6)	1504.66(17)	0.2625
E06	102.465(14)	4.859(7)	16.8784(7)	9.6022(10)	9.2225(7)	1494.69(18)	0.2701
E04	101.753(20)	5.549(10)	16.8551(8)	9.5832(11)	9.2041(7)	1486.70(24)	0.2806
G01	---	5.73(2)**	16.9025(5)	9.6209(3)	9.175(3)	1492.0(5)	0.2610
E05	99.876(13)	6.613(7)	16.8229(9)	9.5590(13)	9.1648(9)	1473.79(28)	0.2913
G02	---	7.84(2) **	15.566(2)	9.625(4)	9.085(5)		
			α= 90.36(4)°	β= 85.90(2)°	γ= 89.16(2)°	1357.5(1.1)	n.d.
F01	---	9.0(1)**	15.496(7)	9.574(3)	9.0377(16)		
			α= 90.02(2)°	β= 85.99(2)°	γ= 88.90(3)°	1337.4(8)	n.d.

Note: distortion parameter $\Delta = 1.094\ (a - \sqrt{3}b)$, Selkregg and Bloss (1980)

‡ at 1 bar, crystal mounted on glass fibre * at 1bar, crystal mounted in DAC without pressure medium

** pressure determined by ruby fluorescence method

[1] after compression in H_2O [2] after compression in argon [3] after compression in ethanol-methanol

Table 3. Data pertaining to the XRD intensity data collections and structure refinement of cordierite compressed in different media

Crystal	Tsi2_b#4	Tsi2_b#4	Tsi2_b#4	Tsi2_b#4	Tsi2_b#4
Medium	air‡	air*	H_2O	H_2O	H_2O
Pressure (GPa)	10^{-4}	10^{-4}	0.39(6)	1.41(8)	1.75(5)
Space group	*Cccm*	*Cccm*	*Cccm*	*Cccm*	*Cccm*
a (Å)	17.089(2)	17.094(2)	17.082(3)	17.029(3)	17.021(3)
b (Å)	9.733(1)	9.691(7)	9.689(7)	9.662(7)	9.659(8)
c (Å)	9.361(1)	9.360(3)	9.346(3)	9.322(3)	9.306(3)
max. 2θ (°)	69.6	69.3	68.5	68.4	69.3
$(\sin\theta/\lambda)_{max}$ ($Å^{-1}$)	0.8030	0.8000	0.7919	0.7909	0.8000
Detector, scan type	CCD, ω/φ	PD, ω	PD, ω	PD, ω	PD, ω
Scan width (°)	0.5	1.2	1.2	1.2	1.2
Scan speed (°/s)	-	0.02	0.02	0.02	0.02
Exposure time (s)	20	-	-	-	-
No. refls.	16112	3162	3215	3171	2951
No. unique refls.	1597	300	259	307	288
with $F_o>4\sigma(F_o)$	1222	229	251	235	217
No. parameter	96	27	27	27	27
R_{int}	0.050	0.083	0.087	0.082	0.084
R_1, $F_o>4\sigma(F_o)$	0.042	0.082	0.092	0.089	0.109
wR^2	0.052	0.116	0.133	0.138	0.141
GooF	1.092	1.427	1.329	1.412	1.541
δe_{max} ($Å^{-3}$)	+0.40	+0.62	+0.69	+1.03	+0.68
δe_{min} ($Å^{-3}$)	-0.39	-0.67	-0.86	-0.88	-0.89

‡ crystal mounted on glass fibre * crystal in DAC

Note: $R_{int} = \Sigma \mid F_{obs}^2 - F_{obs}^2(\text{mean}) \mid / \Sigma [F_{obs}^2]$; $R_1 = \Sigma(|F_{obs}| - |F_{calc}|)/\Sigma|F_{obs}|$; $wR_2 = [\Sigma[w(F^2_{obs} - F^2_{calc})^2]/\Sigma[w(F^2_{obs})^2]]^{0.5}$, $w = 1/ [\sigma^2(F_{obs}^2) + (0.02*P)^2]$, $P = (\text{Max} (F_{obs}^2, 0) +2*F_{calc}^2)/3$

Table 3. (continued)

Crystal	Tsi1#2	Tsi1#2	Tsi1#2	Tsi1#2	Tsi1#2	Tsi1#2	Tsi1#2	Tsi1#2
Medium	air‡	air*	4:1 M-E	4:1 M-E	4:1 M-E	4:1 M-E	4:1 M-E	4:1 M-E
Pressure (GPa)	10^{-4}	10^{-4}	1.07(5)	2.31(5)	3.80(5)	5.20(5)	6.40(5)	6.98(5)
Space group	*Cccm*	*Cccm*	*Cccm*	*Cccm*	*Cccm*	*Cccm*	*Cccm*	*Cccm*
a (Å)	17.060(6)	17.098(16)	17.020(20)	16.973(13)	16.938(14)	16.890(15)	16.842(19)	16.840(16)
b (Å)	9.716(3)	9.698(4)	9.668(7)	9.657(7)	9.652(4)	9.622(4)	9.602(5)	9.583(4)
c (Å)	9.352(2)	9.354(5)	9.294(4)	9.285(5)	9.261(3)	9.215(4)	9.204(3)	9.179(3)
max. 2θ (°)	72.7	78.6	77.9	78.5	78.2	78.2	76.4	78.2
$(\sin\theta/\lambda)_{max}$ ($Å^{-1}$)	0.8340	0.8912	0.8845	0.8902	0.8844	0.8844		
Detector, scan type	CCD, ω/φ	CCD, ω/φ	CCD, ω/φ	CCD, ω/φ	CCD, ω/φ	CCD, ω/φ	CCD, ω/φ	CCD, ω/φ
Scan width (°)	0.5	0.5	0.5	0.5	0.5	0.5	0.5	0.5
Scan speed (°/s)	-	-	-	-	-	-	-	-
Exposure time (s)	20	60	60	60	60	60	60	60
No. refls.	16497	2675	2313	2342	2282	2254	2341	1998
No. unique refls.	1625	718	710	689	688	655	653	636
with $F_o>4\sigma(F_o)$	1294	292	264	264	263	246	242	212
No. parameter	83	30	30	30	30	30	30	30
R_{int}	0.0364	0.0569	0.0497	0.0630	0.0578	0.0549	0.0522	0.0546
R_1 $F_o>4\sigma(F_o)$	0.0678	0.0690	0.0928	0.0648	0.0801	0.0702	0.0960	0.0708
wR^2	0.0553	0.0779	0.1041	0.0798	0.0902	0.0881	0.0872	0.0758
GooF	1.445	1.052	1.121	1.415	1.091	1.122	1.021	1.187
δe_{max} ($Å^{-3}$)	+0.74	+0.52	+0.73	+0.55	+0.64	+0.46	+0.62	+0.80
δe_{min} ($Å^{-3}$)	-0.62	-0.82	-1.12	-0.61	-0.81	-0.56	-0.78	-0.72

Table 4a. Atomic fractional coordinates and displacement parameters (Å^2) of cordierite compressed in 4:1 methanol-ethanol (M-E)

Site	x/a	y/b	z/c	U_{iso}/U_{eq}
10^{-4} GPa (in air)				
M	0.16258(5)	1/2	1/4	0.0067(2)
$T_1$1	1/4	1/4	0.25012(8)	0.0066(2)
$T_1$6	0	1/2	1/4	0.0058(2)
$T_2$1	0.19258(4)	0.07797(8)	0	0.0056(2)
$T_2$3	-0.13523(4)	0.23725(8)	0	0.0055(2)
$T_2$6	0.05084(5)	0.30791(9)	0	0.0056(2)
$O_1$1	0.24739(7)	0.10315(13)	0.14106(12)	0.0081(3)
$O_1$6	0.06215(7)	0.41606(14)	0.15108(12)	0.0084(3)
$O_1$3	-0.17325(7)	0.30997(14)	0.14144(13)	0.0088(3)
$O_2$6	-0.04316(11)	0.24734(21)	0	0.0127(4)
$O_2$1	0.12250(11)	0.18435(21)	0	0.0122(4)
$O_2$3	-0.16462(11)	0.07967(20)	0	0.0118(4)
Ch1 1/4	0.0591(18)	0	1/4	0.07(1)
Ch2 1/4	0	0	1/4	0.08(1)
10^{-4} GPa (in DAC)				
M	0.16247(19)	1/2	1/4	0.0107(7)
$T_1$1	1/4	1/4	0.2504(3)	0.0105(4)
$T_1$6	0	1/2	1/4	0.0105(4)
$T_2$1	0.19259(19)	0.07796(24)	0	0.0105(4)
$T_2$3	-0.1345(2)	0.2371(3)	0	0.0105(4)
$T_2$6	0.0508(2)	0.3088(3)	0	0.0105(4)
$O_1$1	0.2472(3)	0.1024(3)	0.1416(3)	0.0103(6)
$O_1$6	0.0627(2)	0.4178(3)	0.1505(3)	0.0103(6)
$O_1$3	-0.1733(3)	0.3099(3)	0.1423(3)	0.0103(6)
$O_2$6	-0.0423(3)	0.2457(6)	0	0.0103(6)
$O_2$1	0.1228(4)	0.1870(5)	0	0.0103(6)
$O_2$3	-0.1641(5)	0.0793(5)	0	0.0103(6)
Ch1 1/4	0.0359(14)	0	1/4	0.0103(6)
1.07(5) GPa M-E				
M	0.1613(3)	1/2	1/4	0.0139(9)
$T_1$1	1/4	1/4	0.2510(4)	0.0134(4)
$T_1$6	0	1/2	1/4	0.0134(4)
$T_2$1	0.1931(3)	0.0769(3)	0	0.0134(4)
$T_2$3	-0.1346(3)	0.2377(3)	0	0.0134(4)
$T_2$6	0.0520(3)	0.3069(3)	0	0.0134(4)
$O_1$1	0.2472(3)	0.1020(4)	0.1427(4)	0.0119(6)

918	$O_1$6	0.0619(3)	0.4164(5)	0.1498(4)	0.0119(6)
919	$O_1$3	-0.1739(3)	0.3112(4)	0.1420(4)	0.0119(6)
920	$O_2$6	-0.0422(4)	0.2464(7)	0	0.0119(6)
921	$O_2$1	0.1241(5)	0.1858(7)	0	0.0119(6)
922	$O_2$3	-0.1643(7)	0.0806(6)	0	0.0119(6)
923	Ch1 1/4	0.0400(19)	0	1/4	0.0119(6)
924					
925	**2.31(5) GPa M-E**				
926	M	0.16230(19)	1/2	1/4	0.0128(6)
927	$T_1$1	1/4	1/4	0.2513(3)	0.0114(3)
928	$T_1$6	0	1/2	1/4	0.0114(3)
929	$T_2$1	0.1933(2)	0.0778(2)	0	0.0114(3)
930	$T_2$3	-0.1343(2)	0.2370(3)	0	0.0114(3)
931	$T_2$6	0.0514(2)	0.3074(2)	0	0.0114(3)
932	$O_1$1	0.2475(3)	0.1025(3)	0.1418(3)	0.0102(5)
933	$O_1$6	0.0622(3)	0.4163(3)	0.1503(3)	0.0102(5)
934	$O_1$3	-0.1729(3)	0.3100(3)	0.1428(3)	0.0102(5)
935	$O_2$6	-0.0426(3)	0.2428(5)	0	0.0102(5)
936	$O_2$1	0.1223(4)	0.1848(5)	0	0.0102(5)
937	$O_2$3	-0.1655(5)	0.0805(4)	0	0.0102(5)
938	Ch1 1/4	0.0363(14)	0	1/4	0.0102(5)
939					
940	**3.80(5) GPa M-E**				
941	M	0.1622(2)	1/2	1/4	0.0154(8)
942	$T_1$1	1/4	1/4	0.2526(3)	0.0132(4)
943	$T_1$6	0	1/2	1/4	0.0132(4)
944	$T_2$1	0.1945(3)	0.0772(3)	0	0.0132(4)
945	$T_2$3	-0.1335(3)	0.2370(3)	0	0.0132(4)
946	$T_2$6	0.0518(3)	0.3070(3)	0	0.0132(4)
947	$O_1$1	0.2482(3)	0.1024(4)	0.1412(3)	0.0145(7)
948	$O_1$6	0.0623(3)	0.4173(4)	0.1507(4)	0.0145(7)
949	$O_1$3	-0.1727(3)	0.3109(4)	0.1419(4)	0.0145(7)
950	$O_2$6	-0.0416(4)	0.2433(7)	0	0.0145(7)
951	$O_2$1	0.1221(4)	0.1831(6)	0	0.0145(7)
952	$O_2$3	-0.1665(6)	0.0804(5)	0	0.0145(7)
953	Ch1 1/4	0.0397(16)	0	1/4	0.0145(7)
954					
955	**5.20(5) GPa M-E**				
956	M	0.1622(3)	1/2	1/4	0.0183(8)
957	$T_1$1	1/4	1/4	0.2520(3)	0.0159(4)
958	$T_1$6	0	1/2	1/4	0.0159(4)
959	$T_2$1	0.1943(3)	0.0767(3)	0	0.0159(4)
960	$T_2$3	-0.1332(3)	0.2376(3)	0	0.0159(4)
961	$T_2$6	0.0515(3)	0.3066(3)	0	0.0159(4)
962	$O_1$1	0.2483(3)	0.1021(4)	0.1425(4)	0.0166(7)
963	$O_1$6	0.0625(3)	0.4161(4)	0.1507(4)	0.0166(7)

$O_1$3	-0.1723(3)	0.3108(4)	0.1425(4)	0.0166(7)
$O_2$6	-0.0410(4)	0.2404(7)	0	0.0166(7)
$O_2$1	0.1224(5)	0.1841(6)	0	0.0166(7)
$O_2$3	-0.1657(6)	0.0807(6)	0	0.0166(7)
Ch1 1/4	0.0412(17)	0	1/4	0.0166(7)
6.40(5) GPa M-E				
M	0.1618(2)	1/2	1/4	0.0099(8)
$T_1$1	1/4	1/4	0.2528(3)	0.0106(4)
$T_1$6	0	1/2	1/4	0.0106(4)
$T_2$1	0.1952(3)	0.0766(3)	0	0.0106(4)
$T_2$3	-0.1332(3)	0.2371(3)	0	0.0106(4)
$T_2$6	0.0524(3)	0.3061(3)	0	0.0106(4)
$O_1$1	0.2500(3)	0.1015(4)	0.1415(4)	0.0108(6)
$O_1$6	0.0638(3)	0.4174(4)	0.1506(3)	0.0108(6)
$O_1$3	-0.1714(3)	0.3124(4)	0.1426(4)	0.0108(6)
$O_2$6	-0.0409(4)	0.2375(7)	0	0.0108(6)
$O_2$1	0.1236(5)	0.1833(7)	0	0.0108(6)
$O_2$3	-0.1663(6)	0.0815(6)	0	0.0108(6)
Ch1 1/4	0.0355(16)	0	1/4	0.0108(6)
6.98(5) GPa M-E				
M	0.1618(2)	1/2	1/4	0.0119(7)
$T_1$1	1/4	1/4	0.2534(3)	0.0105(4)
$T_1$6	0	1/2	1/4	0.0105(4)
$T_2$1	0.1948(3)	0.0758(3)	0	0.0105(4)
$T_2$3	-0.1334(3)	0.2366(3)	0	0.0105(4)
$T_2$6	0.0522(3)	0.3049(3)	0	0.0105(4)
$O_1$1	0.2497(3)	0.1014(3)	0.1423(3)	0.0141(6)
$O_1$6	0.0637(3)	0.4162(4)	0.1513(3)	0.0141(6)
$O_1$3	-0.1720(3)	0.3128(3)	0.1418(4)	0.0141(6)
$O_2$6	-0.0406(4)	0.2360(6)	0	0.0141(6)
$O_2$1	0.1240(4)	0.1827(6)	0	0.0141(6)
$O_2$3	-0.1687(6)	0.0830(5)	0	0.0141(6)
Ch1 1/4	0.0352(18)	0	1/4	0.0141(6)

Notes: The scattering curve of Mg was used to model the M site, and the refined site occupancy at 0.0001 GPa (in air, and then fixed at any pressure) was 12.72(8)*e*-; the scattering curve of Al was used to model the $T_1$1 and $T_2$6 sites, assuming a full occupancy; the scattering curve of Si was used to model the $T_1$6, $T_2$1 and $T_2$3 sites, assuming a full occupancy; the scattering curve of O was used to model the Ch1 1/4 (*s.o.f.* 1.14(9)*e*-) and Ch2 1/4 (*s.o.f.* 2.2(2)*e*-) sites. The Ch2 1/4 site was not detected at high-pressure conditions. The anisotropic displacement parameter at 0.0001 GPa (in air) are available in the CIF. For the H*P* structure refinements, the following constrains were applied: *U*iso($T_1$1)=*U*iso($T_1$6)=*U*iso ($T_2$1)=*U*iso($T_2$3)=*U*iso($T_2$6) and *U*iso($O_1$1)=*U*iso ($O_1$6)=*U*iso($O_1$3)=*U*iso($O_2$6)=*U*iso($O_2$1)=*U*iso($O_2$3)=*U*iso(Ch1 ¼).

Table 4b. Atomic fractional coordinates and displacement parameters (Å^2) of cordierite compressed in H_2O.

Site	x/a	y/b	z/c	U_{iso}/U_{eq}
10^{-4} GPa (in air)				
M	0.16255(4)	1/2	1/4	0.0075(2)
$T_1$1	1/4	1/4	0.25015(9)	0.0075(2)
$T_1$6	0	1/2	1/4	0.0068(3)
$T_2$1	0.19259(3)	0.07771(6)	0	0.0058(2)
$T_2$3	-0.13517(3)	0.23739(6)	0	0.0061(2)
$T_2$6	0.05094(4)	0.30813(7)	0	0.0088(2)
$O_1$1	0.24731(6)	0.10303(10)	0.14108(12)	0.0131(3)
$O_1$6	0.06229(6)	0.41632(11)	0.15122(12)	0.0129(3)
$O_1$3	-0.17330(6)	0.31009(11)	0.14163(13)	0.0136(3)
$O_2$6	-0.04314(8)	0.24833(17)	0	0.0174(4)
$O_2$1	0.12246(8)	0.18494(16)	0	0.0170(4)
$O_2$3	-0.16466(9)	0.07955(15)	0	0.0161(4)
Ch1 1/4	-0.05980	0	1/4	0.11(1)
Ch2 1/4	0	0	1/4	0.07(1)
Na	0	0	0	0.04(1)
10^{-4} GPa (in DAC)				
M	0.16264(19)	1/2	1/4	0.0011(10)
$T_1$1	1/4	1/4	0.2500(6)	0.0044(5)
$T_1$6	0	1/2	1/5	0.0044(5)
$T_2$1	0.19240(19)	0.0776(7)	0	0.0044(5)
$T_2$3	-0.1353(2)	0.2372(7)	0	0.0044(5)
$T_2$6	0.0510(2)	0.3086(7)	0	0.0044(5)
$O_1$1	0.2463(3)	0.1018(7)	0.1423(6)	0.0104(10).
$O_1$6	0.0622(2)	0.4173(9)	0.1503(6)	0.0104(10).
$O_1$3	-0.1734(3)	0.3087(7)	0.1430(6)	0.0104(10).
$O_2$6	-0.0434(4)	0.2484(15)	0	0.0104(10)
$O_2$1	0.1225(4)	0.1853(11)	0	0.0104(10)
$O_2$3	-0.1657(5)	0.0798(9)	0	0.0104(10)
0.39(6) GPa H_2O				
M	0.1622(2)	1/2	1/4	0.0056(12)
$T_1$1	1/4	1/4	0.2501(5)	0.0031(5)
$T_1$6	0	1/2	1/4	0.0031(5)
$T_2$1	0.1926(2)	0.0779(7)	0	0.0031(5)
$T_2$3	-0.1353(2)	0.2372(7)	0	0.0031(5)
$T_2$6	0.0507(2)	0.3081(7)	0	0.0031(5)
$O_1$1	0.2471(4)	0.1023(8)	0.1413(6)	0.0058(11)

$O_1$6	0.0623(3)	0.4159(9)	0.1512(7)	0.0058(11)
$O_1$3	-0.1735(3)	0.3094(7)	0.1414(6)	0.0058(11)
$O_2$6	-0.0427(4)	0.2444(16)	0	0.0058(11)
$O_2$1	0.1223(5)	0.1846(13)	0	0.0058(11)
$O_2$3	-0.1651(6)	0.0792(9)	0	0.0058(11)
1.41(8) GPa H_2O				
M	0.1625(2)	1/2	1/4	0.0053(12)
$T_1$1	1/4	1/4	0.2506(7)	0.0056(6)
$T_1$6	0	1/2	1/4	0.0056(6)
$T_2$1	0.1933(2)	0.0768(7)	0	0.0056(6)
$T_2$3	-0.1349(2)	0.2367(7)	0	0.0056(6)
$T_2$6	0.0514(2)	0.3088(7)	0	0.0056(6)
$O_1$1	0.2471(4)	0.1025(8)	0.1420(8)	0.0076(11)
$O_1$6	0.0623(3)	0.4142(9)	0.1526(7)	0.0076(11)
$O_1$3	-0.1735(3)	0.3101(7)	0.1401(6)	0.0076(11)
$O_2$6	-0.0419(4)	0.2446(16)	0	0.0076(11)
$O_2$1	0.1235(5)	0.1858(12)	0	0.0076(11)
$O_2$3	-0.1653(6)	0.0793(9)	0	0.0076(11)
1.75(5) GPa H_2O				
M	0.1626(3)	1/2	1/4	0.0081(14)
$T_1$1	1/4	1/4	0.2496(7)	0.0073(7)
$T_1$6	0	1/2	1/4	0.0073(7)
$T_2$1	0.1931(3)	0.0773(8)	0	0.0073(7)
$T_2$3	-0.1346(3)	0.2368(8)	0	0.0073(7)
$T_2$6	0.0512(3)	0.3065(8)	0	0.0073(7)
$O_1$1	0.2471(4)	0.1023(9)	0.1417(7)	0.0091(13)
$O_1$6	0.0622(3)	0.4139(11)	0.1522(9)	0.0091(13)
$O_1$3	-0.1729(4)	0.3075(8)	0.1424(7)	0.0091(13)
$O_2$6	-0.0424(5)	0.2464(20)	0	0.0091(13)
$O_2$1	0.1234(6)	0.1858(14)	0	0.0091(13)
$O_2$3	-0.1660(7)	0.0805(11)	0	0.0091(13)

Notes: The scattering curve of Mg was used to model the M site, and the refined site occupancy at 0.0001 GPa (in air, and then fixed at any pressure) was 12.00(4)*e*-; the scattering curve of Al was used to model the $T_1$1 and $T_2$6 sites, assuming a full occupancy; the scattering curve of Si was used to model the $T_1$6, $T_2$1 and $T_2$3 sites, assuming a full occupancy; the scattering curve of O was used to model the Ch1 1/4 (*s.o.f.* 1.6(2)*e*-) and Ch2 1/4 (*s.o.f.* 2.2(3)*e*-) sites and that of sodium for the Na site (*s.o.f.* 0.45(7)*e*-). All the channel sites were not detected with the crystal in the DAC. The anisotropic displacement parameter at 0.0001 GPa (in air) are available in the CIF. For the H*P* structure refinements, the following constrains were applied: *U*iso($T_1$1)=*U*iso($T_1$6)=*U*iso($T_2$1)=*U*iso($T_2$3)=*U*iso($T_2$6) and *U*iso($O_1$1)=*U*iso($O_1$6)=*U*iso($O_1$3)=*U*iso($O_2$6)=*U*iso($O_2$1)=*U*iso($O_2$3)=*U*iso(Ch1 ¼).

Table 5a. Selected bond distances (Å), ring "diameters" (Å) and other structural parameters of cordierite compressed in methanol-ethanol mix at different pressures.

P (GPa),	0.0001	0.0001*	1.07(5)	2.31(5)
M-$O_1$1 (×2)	2.098(2)	2.098(5)	2.095(7)	2.081(5)
M-$O_1$6 (×2)	2.111(2)	2.101(5)	2.093(7)	2.097(5)
M-$O_1$3 (×2)	2.115(2)	2.109(4)	2.094(4)	2.095(3)
<M-O>	2.108	2.103	2.094	2.091
$T_1$1-$O_1$3 (×2)	1.756(2)	1.750(5)	1.737(6)	1.750(4)
$T_1$1-$O_1$1 (×2)	1.754(2)	1.757(4)	1.751(5)	1.736(4)
<$T_1$1-O>	1.755	1.754	1.744	1.743
$T_1$6-$O_1$6 (×4)	1.626(2)	1.628(4)	1.622(5)	1.620(4)
$T_2$1-$O_2$1	1.580(3)	1.594(7)	1.578(9)	1.587(7)
$T_2$1-$O_2$3	1.604(3)	1.601(6)	1.599(8)	1.600(6)
$T_2$1-$O_1$1 (×2)	1.635(2)	1.638(4)	1.633(6)	1.625(5)
<$T_2$1-O>	1.614	1.618	1.611	1.609
$T_2$3-$O_2$6	1.574(2)	1.577(8)	1.574(9)	1.557(7)
$T_2$3-$O_2$3	1.611(3)	1.612(6)	1.601(8)	1.601(6)
$T_2$3-$O_1$3 (×2)	1.634(2)	1.646(4)	1.642(5)	1.638(4)
<$T_2$3-O>	1.613	1.620	1.615	1.609
$T_2$6-$O_2$6	1.708(3)	1.706(7)	1.708(9)	1.714(7)
$T_2$6-$O_2$1	1.713(3)	1.707(7)	1.695(9)	1.688(7)
$T_2$6-$O_1$6 (×2)	1.771(2)	1.772(4)	1.757(5)	1.757(4)
<$T_2$6-O>	1.741	1.739	1.729	1.729
$O_2$3 ↔ $O_2$3	5.826(3)	5.819(13)	5.806(18)	5.829(12)
$O_2$6 ↔ $O_2$6	5.026(3)	4.980(8)	4.976(10)	4.905(8)
$O_2$1 ↔ $O_2$1	5.504(3)	5.549(9)	5.545(12)	5.478(9)
$\varepsilon_{[001]}$	0.904(1)	0.905(2)	0.906(3)	0.891(2)
$T_2$1-$O_2$1-$T_2$6	176.3(1)	177.7(4)	178.2(6)	176.2(4)
$T_2$3-$O_2$3-$T_2$1	179.2(1)	179.4(4)	179.4(5)	177.8(3)
$T_2$6-$O_2$6-$T_2$3	163.4(1)	162.0(4)	163.0(5)	160.6(4)
$O_2$6-$O_2$3-$O_2$1	112.51(9)	112.5(3)	112.8(3)	111.0(2)
$O_2$3-$O_2$1-$O_2$6	117.87(9)	116.7(3)	116.6(4)	117.2(3)
$O_2$1-$O_2$6-$O_2$3	129.62(9)	130.8(3)	130.7(4)	131.8(3)
V_{polMg},	11.77(2)	11.68(5)	11.53(6)	11.48(5)
ξ	0.0574	0.0576	0.0591	0.0586

P (GPa),	3.80(5)	5.20(5)	6.40(5)	6.98(5)
M-$O_1$1 (×2)	2.073(6)	2.057(6)	2.038(6)	2.035(6)
M-$O_1$6 (×2)	2.085(6)	2.079(6)	2.047(6)	2.047(6)
M-$O_1$3 (×2)	2.090(4)	2.079(4)	2.061(4)	2.058(4)
<M-O>	2.083	2.072	2.049	2.047
$T_1$1-$O_1$3 (×2)	1.737(5)	1.735(5)	1.742(5)	1.735(5)
$T_1$1-$O_1$1 (×2)	1.760(4)	1.745(5)	1.756(5)	1.752(4)
<$T_1$1-O>	1.749	1.740	1.749	1.744
$T_1$6-$O_1$6 (×4)	1.612(5)	1.613(5)	1.618(5)	1.618(5)
$T_2$1-$O_2$1	1.596(8)	1.594(8)	1.582(8)	1.572(8)
$T_2$1-$O_2$3	1.593(7)	1.589(7)	1.594(7)	1.584(7)
$T_2$1-$O_1$1 (×2)	1.611(5)	1.618(5)	1.613(5)	1.619(5)
<$T_2$1-O>	1.603	1.605	1.601	1.599
$T_2$3-$O_2$6	1.558(9)	1.559(9)	1.554(8)	1.562(8)
$T_2$3-$O_2$3	1.611(7)	1.606(7)	1.595(8)	1.587(7)
$T_2$3-$O_1$3 (×2)	1.635(5)	1.630(5)	1.631(5)	1.628(5)
<$T_2$3-O>	1.610	1.606	1.603	1.601
$T_2$6-$O_2$6	1.698(9)	1.687(9)	1.705(8)	1.697(8)
$T_2$6-$O_2$1	1.687(8)	1.680(8)	1.682(8)	1.684(8)
$T_2$6-$O_1$6 (×2)	1.764(4)	1.753(5)	1.761(4)	1.762(4)
<$T_2$6-O>	1.728	1.718	1.727	1.726
$O_2$3 ↔ $O_2$3	5.850(15)	5.809(15)	5.816(15)	5.897(15)
$O_2$6 ↔ $O_2$6	4.904(10)	4.829(8)	4.764(10)	4.725(8)
$O_2$1 ↔ $O_2$1	5.441(9)	5.445(9)	5.452(10)	5.453(10)
$\varepsilon_{[001]}$	0.887(3)	0.878(3)	0.879(3)	0.875(3)
$T_2$1-$O_2$1-$T_2$6	174.7(5)	175.9(5)	175.8(5)	176.7(5)
$T_2$3-$O_2$3-$T_2$1	177.0(4)	177.7(5)	177.3(5)	174.2(4)
$T_2$6-$O_2$6-$T_2$3	161.0(5)	158.8(5)	157.4(5)	156.9(5)
$O_2$6-$O_2$3-$O_2$1	110.2(3)	110.1(3)	109.6(3)	107.8(3)
$O_2$3-$O_2$1-$O_2$6	118.3(3)	117.1(3)	116.4(3)	116.8(3)
$O_2$1-$O_2$6-$O_2$3	131.5(4)	132.8(4)	134.0(4)	135.3(4)
V_{polMg}	11.36(5)	11.17(5)	10.86(5)	10.81(5)
ξ	0.0567	0.0586	0.0529	0.0548

*Note*s. Ellipticity ratio: $\varepsilon_{[001]} = 0.5\cdot[(O_2 6 \leftrightarrow O_2 6) + (O_2 1 \leftrightarrow O_2 1)]/[O_2 3 \leftrightarrow O_2 3]$; Mg-polyhedral volume ($V_{polMg}$, Å^3) and polyhedral distortion coefficient (ξ, dimensionless) according to Balic-Zunic and Vickovic (1996) and Makovicky and Balic-Zunic (1998). * Crystal in the DAC without *P*-medium.

Table 5b. Selected bond distances (Å), ring "diameters" (Å) and other structural parameters of cordierite compressed in H_2O at different pressures. (* Crystal in the DAC without *P*-medium).

P (GPa),	0.0001	0.0001*	0.39(6)	1.41(8)	1.75(5)
M-$O_1$1 (×2)	2.102(1)	2.100(5)	2.102(5)	2.089(6)	2.087(6)
M-$O_1$6 (×2)	2.110(1)	2.112(5)	2.105(5)	2.103(5)	2.106(5)
M-$O_1$3 (×2)	2.117(1)	2.115(6)	2.116(6)	2.110(6)	2.119(6)
<M-O>	2.110	2.109	2.108	2.101	2.104
$T_1$1-$O_1$3 (×2)	1.757(1)	1.745(5)	1.751(5)	1.753(5)	1.742(6)
$T_1$1-$O_1$1 (×2)	1.758(1)	1.756(6)	1.756(6)	1.749(6)	1.745(6)
<$T_1$1-O>	1.7575	1.7505	1.7535	1.7510	1.7435
$T_1$6-$O_1$6 (×4)	1.628(1)	1.626(4)	1.627(4)	1.624(4)	1.625(4)
$T_2$1-$O_2$1	1.589(1)	1.586(7)	1.584(7)	1.588(7)	1.583(8)
$T_2$1-$O_2$3	1.603(2)	1.592(8)	1.593(8)	1.582(8)	1.593(8)
$T_2$1-$O_1$1 (×2)	1.637(1)	1.637(5)	1.633(5)	1.628(5)	1.626(5)
<$T_2$1-O>	1.6165	1.6130	1.6108	1.6065	1.6070
$T_2$3-$O_2$6	1.576(1)	1.575(6)	1.583(6)	1.586(7)	1.573(7)
$T_2$3-$O_2$3	1.617(2)	1.612(8)	1.614(8)	1.606(8)	1.602(9)
$T_2$3-$O_1$3 (×2)	1.638(1)	1.641(5)	1.632(5)	1.624(5)	1.627(5)
<$T_2$3-O>	1.6173	1.6173	1.6152	1.6100	1.6073
$T_2$6-$O_2$6	1.710(1)	1.715(6)	1.711(7)	1.707(7)	1.695(8)
$T_2$6-$O_2$1	1.712(2)	1.709(7)	1.711(7)	1.708(7)	1.694(8)
$T_2$6-$O_1$6 (×2)	1.775(1)	1.768(5)	1.768(5)	1.760(5)	1.766(4)
<$T_2$6-O>	1.7430	1.7400	1.7395	1.7338	1.7303
$O_2$3 ↔ $O_2$3	5.837(2)	5.872(12)	5.846(14)	5.835(14)	5.861(17)
$O_2$6 ↔ $O_2$6	5.054(2)	5.038(20)	4.956(21)	4.937(21)	4.967(27)
$O_2$1 ↔ $O_2$1	5.521(2)	5.517(12)	5.503(15)	5.530(15)	5.527(17)
$\varepsilon_{[001]}$	0.906(1)	0.899(4)	0.894(4)	0.897(4)	0.895(6)
$T_2$1-$O_2$1-$T_2$6	176.6(1)	176.8(6)	176.4(7)	177.4(7)	178.0(8)
$T_2$3-$O_2$3-$T_2$1	179.2(1)	177.8(7)	178.7(7)	178.7(8)	177.3(8)
$T_2$6-$O_2$6-$T_2$3	163.9(1)	164.1(5)	161.4(5)	161.4(5)	163.1(6)
$O_2$6-$O_2$3-$O_2$1	112.7(7)	111.9(5)	111.5(5)	111.7(5)	111.5(6)
$O_2$3-$O_2$1-$O_2$6	117.95(7)	118.2(4)	117.5(4)	116.9(5)	117.4(5)
$O_2$1-$O_2$6-$O_2$3	129.35(7)	129.8(3)	130.9(4)	131.4(4)	131.2(5)
V_{polMg}	11.80(1)	11.76(6)	11.75(7)	11.63(7)	11.66(8)
ξ	0.0578	0.0600	0.0580	0.0587	0.0617

Table 6. Results of the fits for the pressure dependencies of the crystallographic axes and the Birch-Murnaghan equation of state.

V (Å^3); a,b,c (Å)	$K_{T=298}$, β_i^{-1} (GPa)	$\partial K/\partial P$, $\partial(\beta_i^{-1})/\partial P$	χ^2_w	$\lvert P_{obs} - P_{calc} \rvert$ (GPa)
cordierite in H_2O (10^{-4} to 2.01 GPa)				
V_0 = 1551.83(3)	$K_{T=298}$ = 137.8(1.5)	$\partial K/\partial$P = -6.4(1.8)	1.35	≤ 0.011
a_0 = 17.0732(2)	1/3 β_a^{-1} = 150.8(2.7)	1/3 $\partial(\beta_a^{-1})/\partial$P = -5.1(3.0)	1.16	≤ 0.019
b_0 = 9.7243(2)	1/3 β_b^{-1} = 146.8(4.4)	1/3 $\partial(\beta_b^{-1})/\partial$P = -2.3(4.9)	2.31	≤ 0.051
c_0 = 9.3483(2)	1/3 β_c^{-1} = 105.2(1.6)	1/3 $\partial(\beta_c^{-1})/\partial$P = 4.5(1.9)	0.95	≤ 0.013
cordierite in argon (10^{-4} to 6.44 GPa)				
V_0 = 1550.56(15)	$K_{T=298}$ = 127.7(2.3)	$\partial K/\partial$P = 0.4(0.9)	3.54	≤ 0.026
a_0 = 17.0728(7)	1/3 β_a^{-1} = 117.9(2.3)	1/3 $\partial(\beta_a^{-1})/\partial$P = 11.2(1.3)	2.63	≤ 0.012
b_0 = 9.7198(4)	1/3 β_b^{-1} = 148.1.(2.8)	1/3 $\partial(\beta_b^{-1})/\partial$P = -4.3(0.9)	1.04	≤ 0.053
c_0 = 9.3437(6)	1/3 β_c^{-1} = 116.1(2.4)	1/3 $\partial(\beta_c^{-1})/\partial$P = -1.2(0.8)	3.00	≤ 0.023
cordierite in ethanol-methanol (10^{-4} to 6.61 GPa)				
V_0 = 1551.97(15)	$K_{T=298}$ = 131.0(1.3)	$\partial K/\partial$P = -0.5(0.4)	0.83	≤ 0.008
a_0 = 17.0722(8)	1/3 β_a^{-1} = 121.7(2.2)	1/3 $\partial(\beta_a^{-1})/\partial$P = 9.3(9)	1.66	≤ 0.005
b_0 = 9.726(6)	1/3 β_b^{-1} = 133.4(7.8)	1/3 $\partial(\beta_b^{-1})/\partial$P = -1.9(1.9)	5.83	≤ 0.067
c_0 = 9.348(2)	1/3 β_c^{-1} = 129.9(4.9)	1/3 $\partial(\beta_c^{-1})/\partial$P = -3.5(1.0)	11.3	≤ 0.047

Figures and Figure Captions

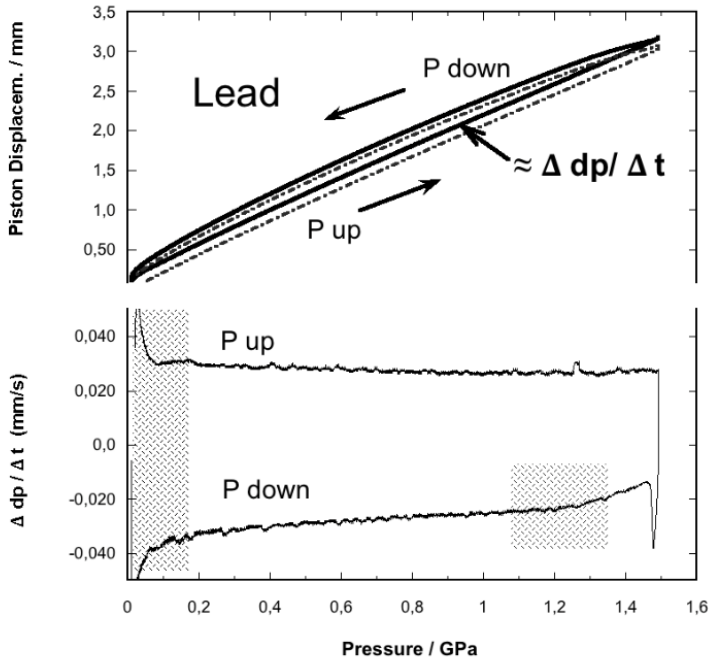

Figure 1. Compression experiment of lead up to 1.5 GPa as calibration reference for the performed compression experiments on cordierite. Top: the solid line gives the loop (piston displacement versus pressure) obtained from compression (*P* up) - decompression (*P* down) run. The adjacent loop (dotted-dashed line) represents the dp-*P*-loop displaced by Δt (usually 15 seconds, here for better presentation Δt = 200 s). Bottom: the Δdp/Δt-parameter plotted versus pressure. The hatched areas indicate regions of strong influences by the characteristics of the high-pressure apparatus (apparatus function).

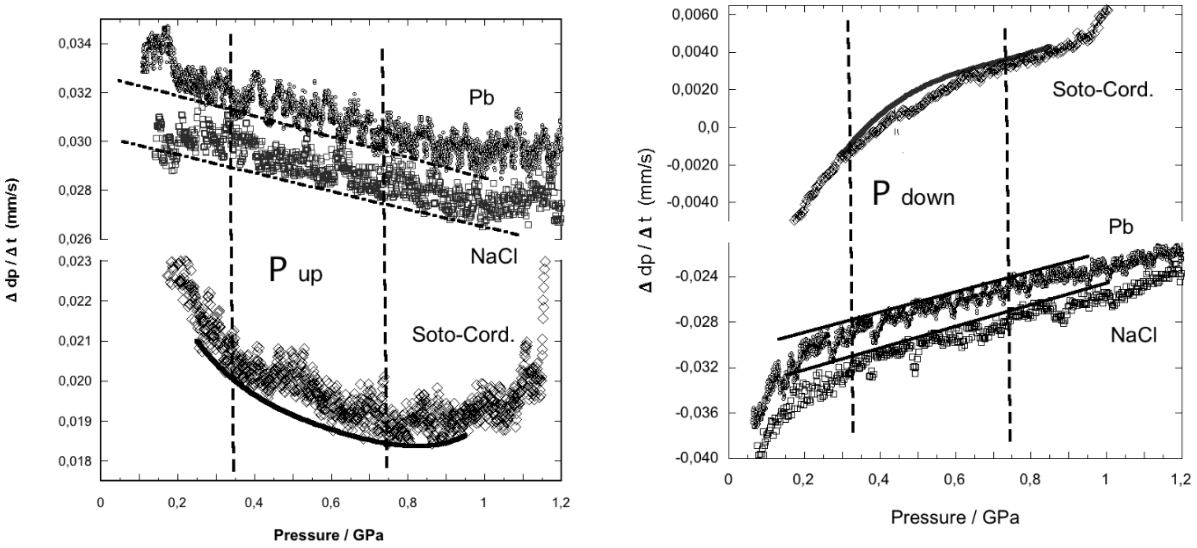

Figure 2. (*Left side*) The Δdp/Δ*t* parameter derived from a compression run of Soto cordierite plotted versus pressure in comparison with Δdp/Δ*t* data obtained from calibration runs on lead and NaCl.
(*Right side*) The equivalent data obtained on decompression. While the reference materials lead and NaCl exhibit a linear behavior of the Δdp/Δ*t*-parameter, the Soto cordierite reveals in each track two subtle irregularities at around 0.3 and 0.75 GPa encompassing a deviation n from the general compression trend (line as a guide to the eye).

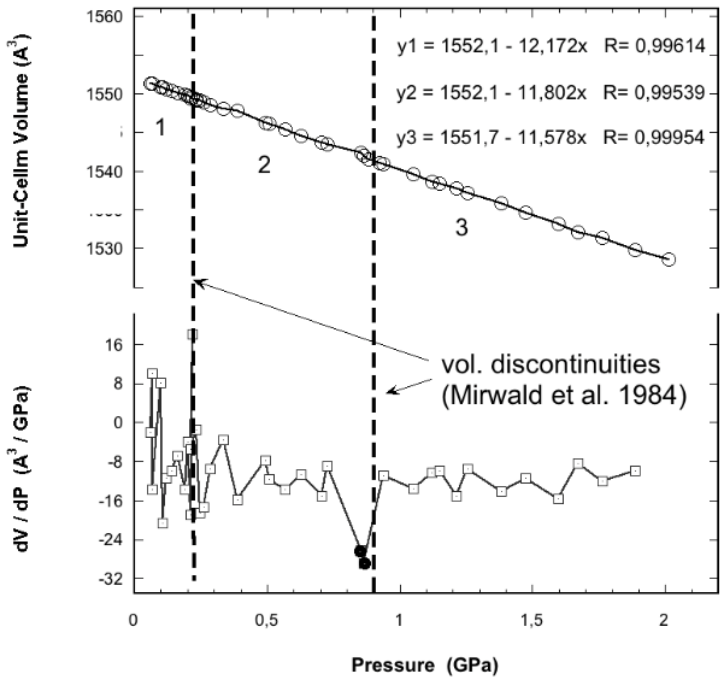

Figure 3. Cell volume (top) and compression coefficient d*V*/d*P* (bottom) obtained from cordierite (Tsi2_b#3) pressurized in DAC with water as pressure medium. The d*V*/d*P* data give a vague hint for irregularities at around 0.35 and 0.85 GPa, which is next to the supposed volume discontinuities previously reported. Linear fits to the volume data truncated to the three sections (1,2, and 3) yield differences in the slope of about 2%.

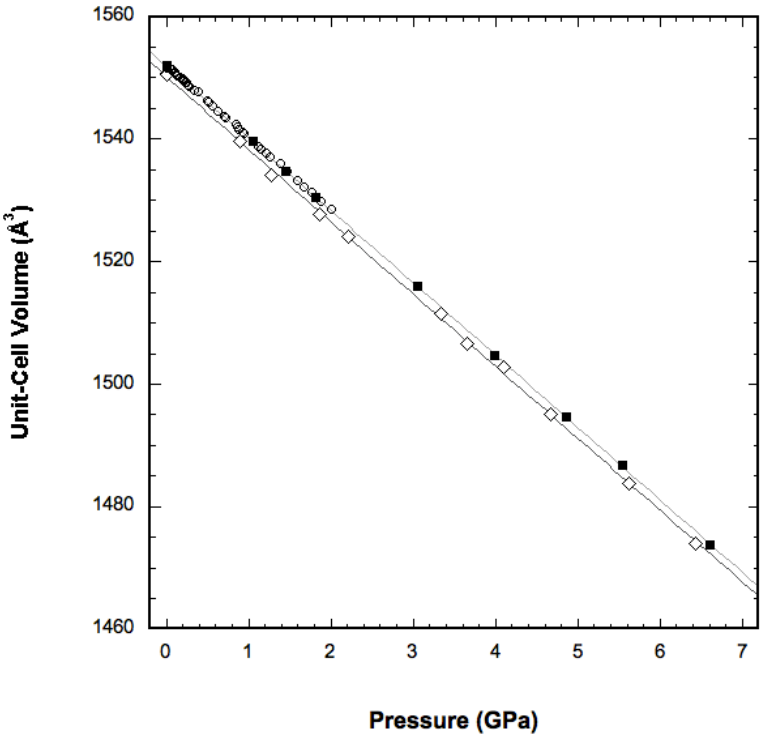

Figure 4. Unit-cell volumes from single-crystal XRD of cordierite in H_2O (open circles), in argon (open diamonds), and 4:1 methanol-ethanol (full squares). Lines correspond to the fit of a third-order Birch-Murnaghan EoS to the individual *P*-*V* data sets.

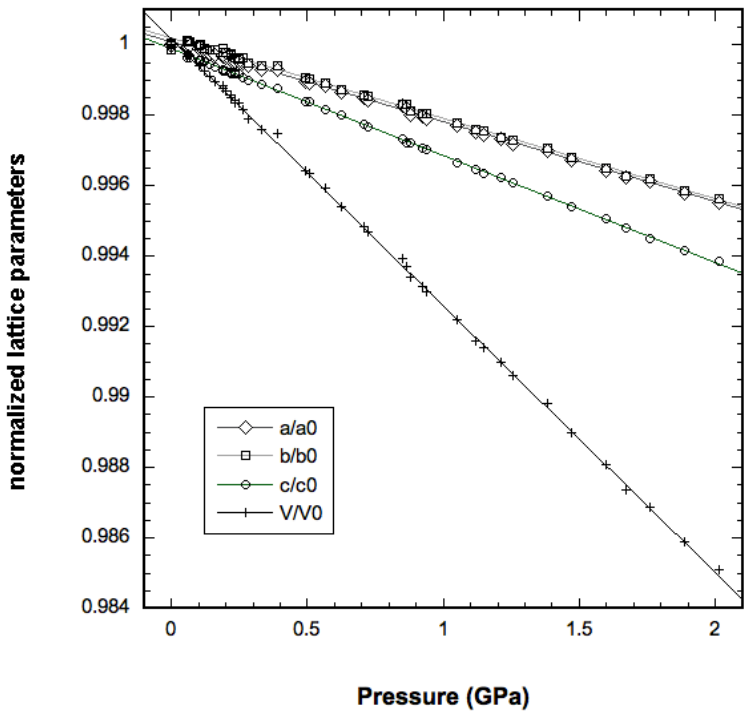

Figure 5. Lattice parameters *a*, *b*, *c* and unit-cell volume *V* of cordierite in H_2O (in the hydrostatic pressure range 10^{-4} to 2.01 GPa). a/a_0 (open diamonds), b/b_0 (open squares), c/c_0 (open circles), and V/V_0 (crosses). Plotted lines correspond to linear fits with β_i^{-1} (i = *a*, *b*, *c*) = 440.0, 438.3, 328.7 GPa and K_0= 132.1 GPa, respectively.

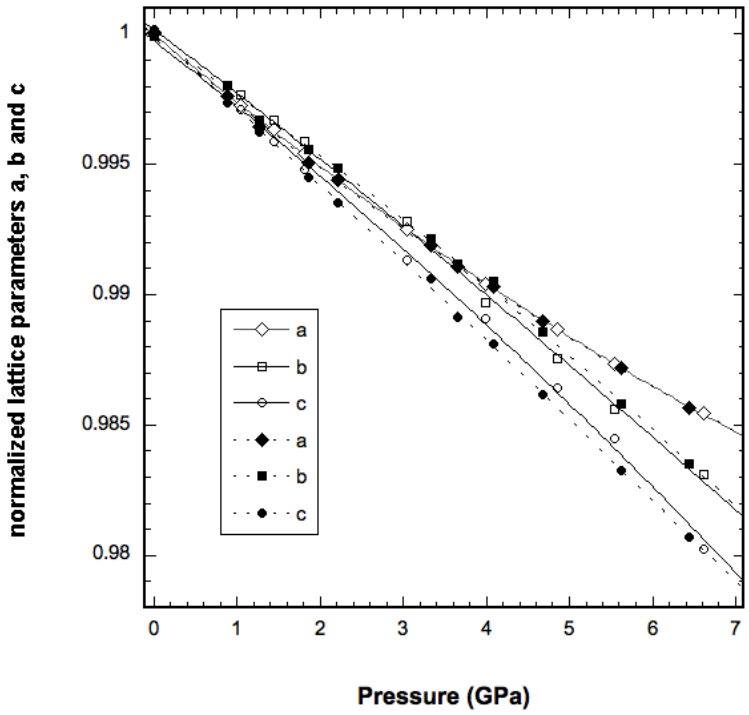

Figure 6. Lattice parameters *a, b, and c* of cordierite in methanol-ethanol mix (open symbols) and argon (full symbols). Plotted data correspond to normalized parameter a/a_0 (diamonds), b/b_0 (squares), c/c_0 (circles); lines correspond to fits of a Birch-Murnaghan EoS with axial moduli β_i^{-1} (i = *a*, *b*, *c*) and their pressure derivatives $\partial(\beta_i^{-1})/\partial P$ (see Table 6).

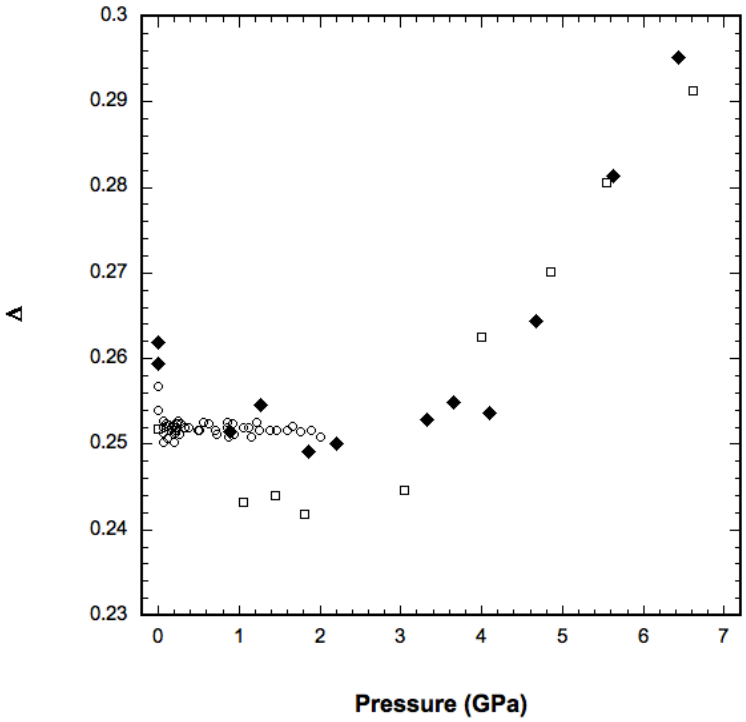

Figure 7. Evolution of the distortion index Δ (°) = 1.094 (a - √3b) (Miyashiro, 1957) with pressure for the data of cordierite compressed in H_2O (open circles), argon (full diamonds) and methanol-ethanol mixture (open squares). Note the significant change in the trend with Δ starting to increase with pressure above ~4 GPa.

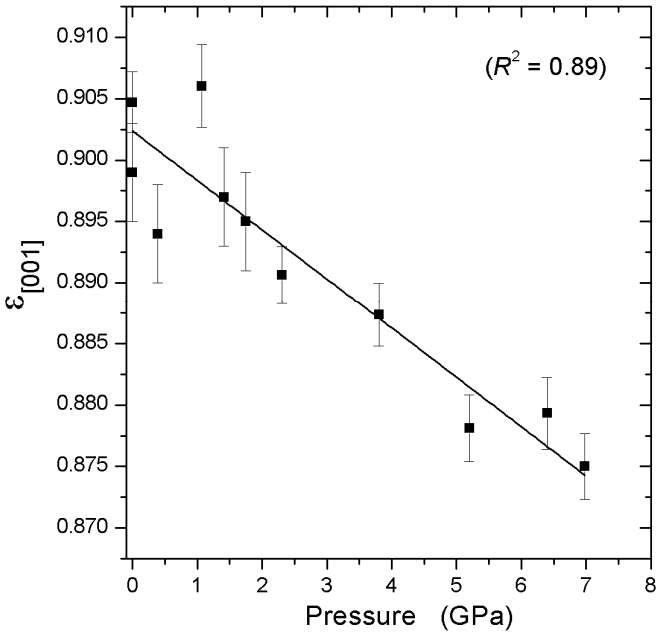

1348 (a)
1349

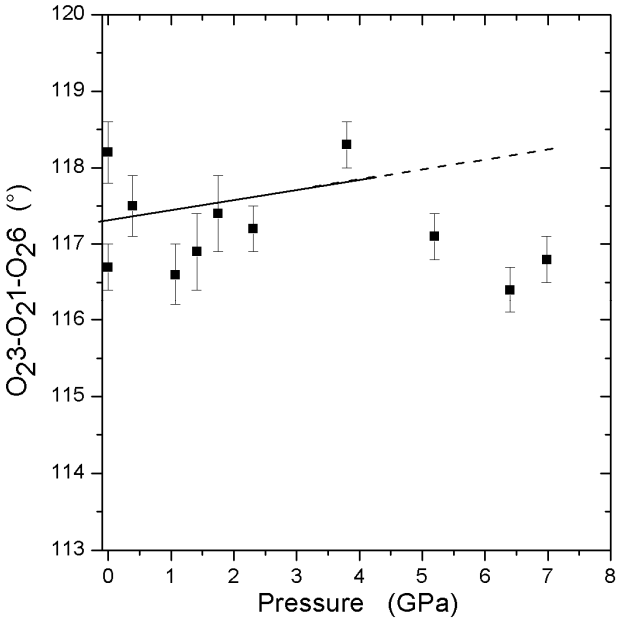

1350 (b)

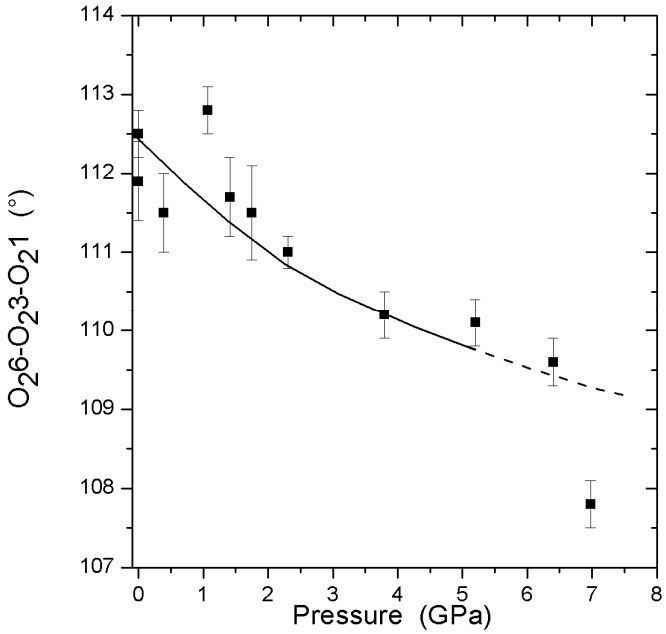

(c)

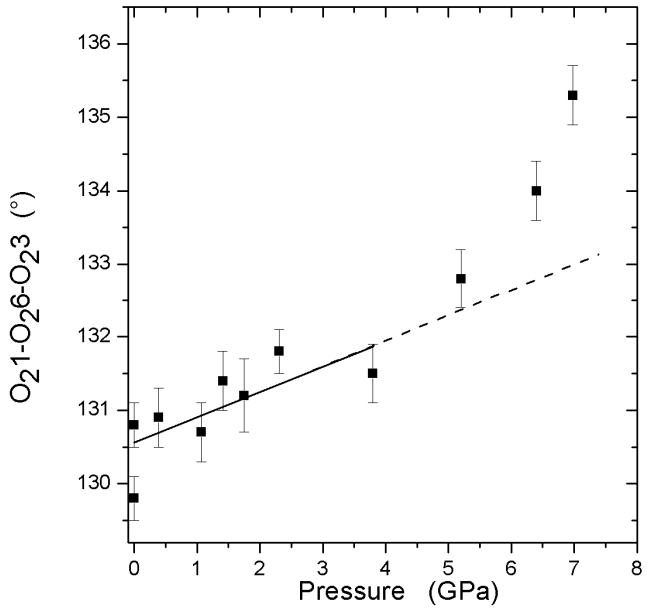

(d)

Figure 8. (a) Evolution of the ellipticity ratio of the 6-membered rings of tetrahedra running along [001] (i.e. $\varepsilon_{[001]}$) and of the inter-tetrahedral angles (b) O_26-O_23-O_21, (c) O_23-O_21-O_26, and (d) O_21-O_26-O_23 (°) with pressure. Lines represent the trends of evolution with pressure.

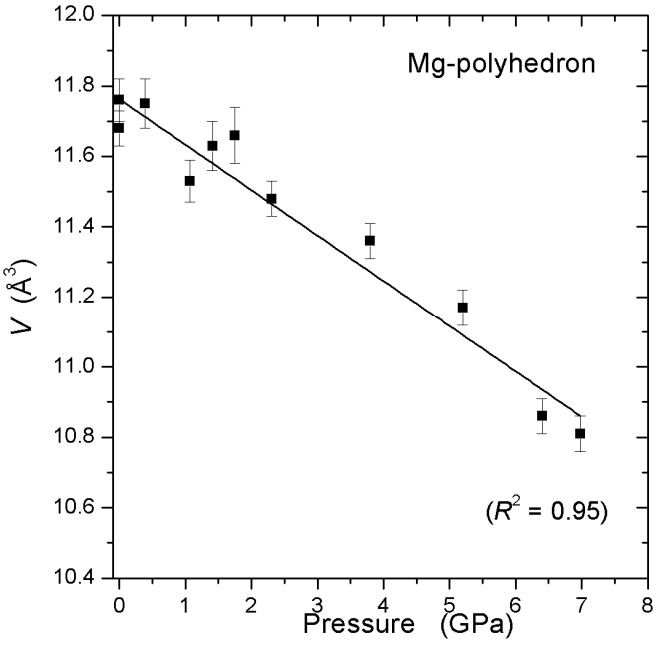

(a)

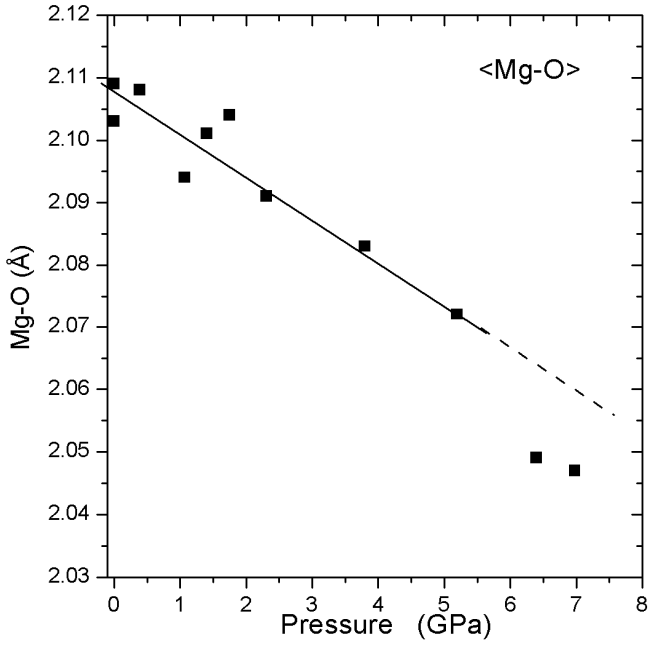

(b)

Figure 9. Evolution of (a) the polyhedral volume and (b) of the average <Mg-O> bond distances (see Table 5) of the Mg-octahedron with pressure. Lines represent the trends of evolution with *P*.

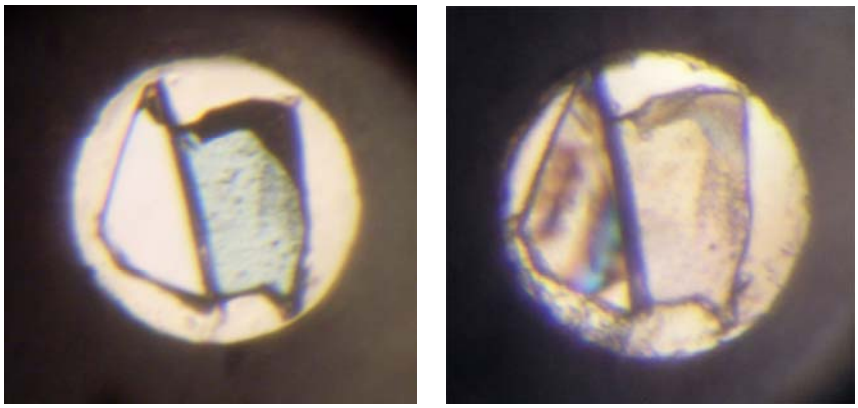

Figure 10. Cordierite single crystal (sample Tsi2_b#1, crystal on the left side) mounted together with quartz pressure standard (right side) below (~1.3 GPa) and above (~7.2 GPa) the transition at ~6.9 GPa (pressure medium: argon). Note the interference colors and gradual changes indicating strain across domain boundaries according to the orthorhombic-to-triclinic transition in comparison to the homogeneous single-domain crystal of orthorhombic symmetry at low pressure (image detail: 300 μm x 300 μm).

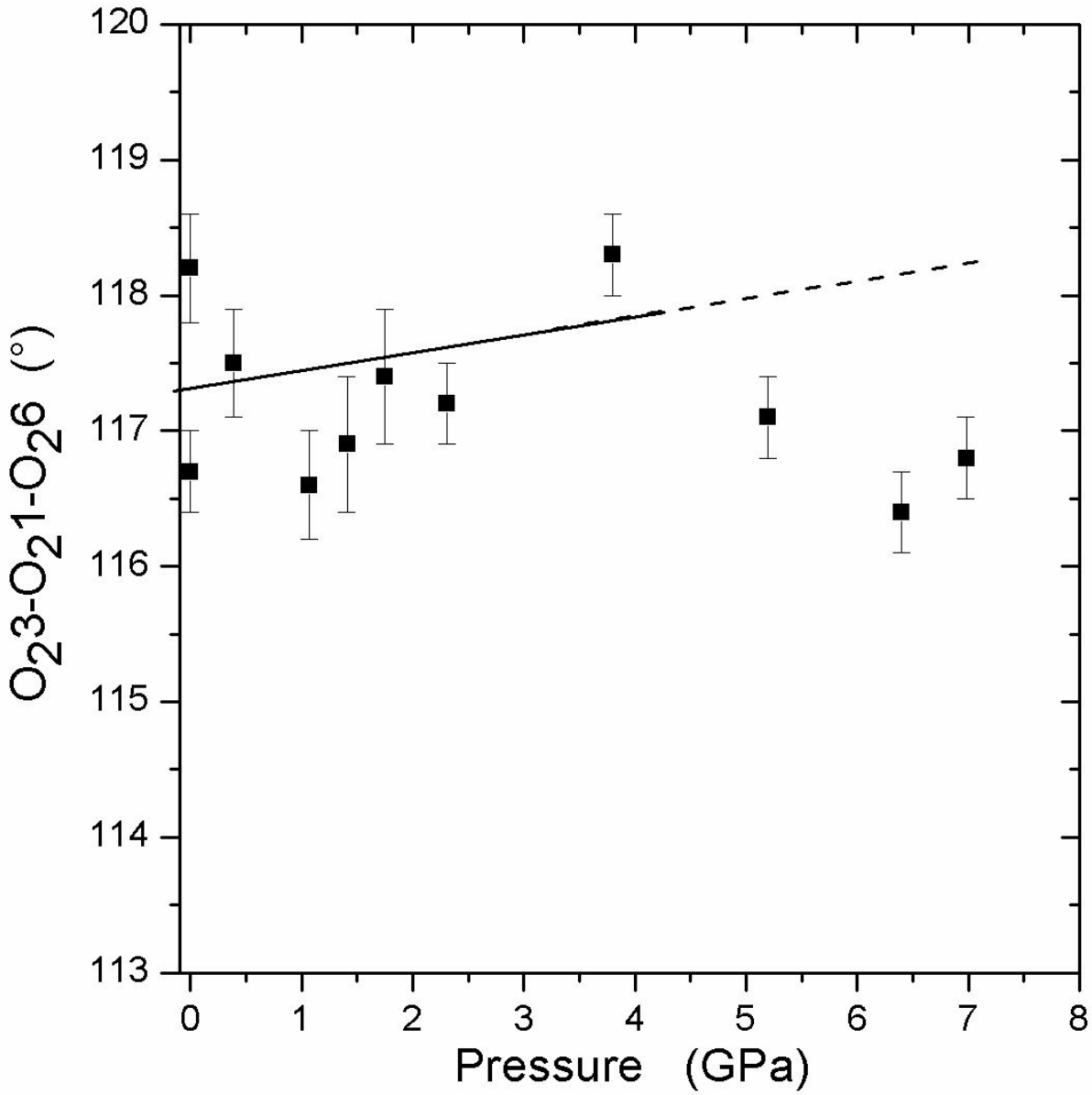
120
119
118
117
116
115
114
113
0
1
2
3
4
5
6
7
8
Pressure (GPa)
O23-O21-O26 (°)

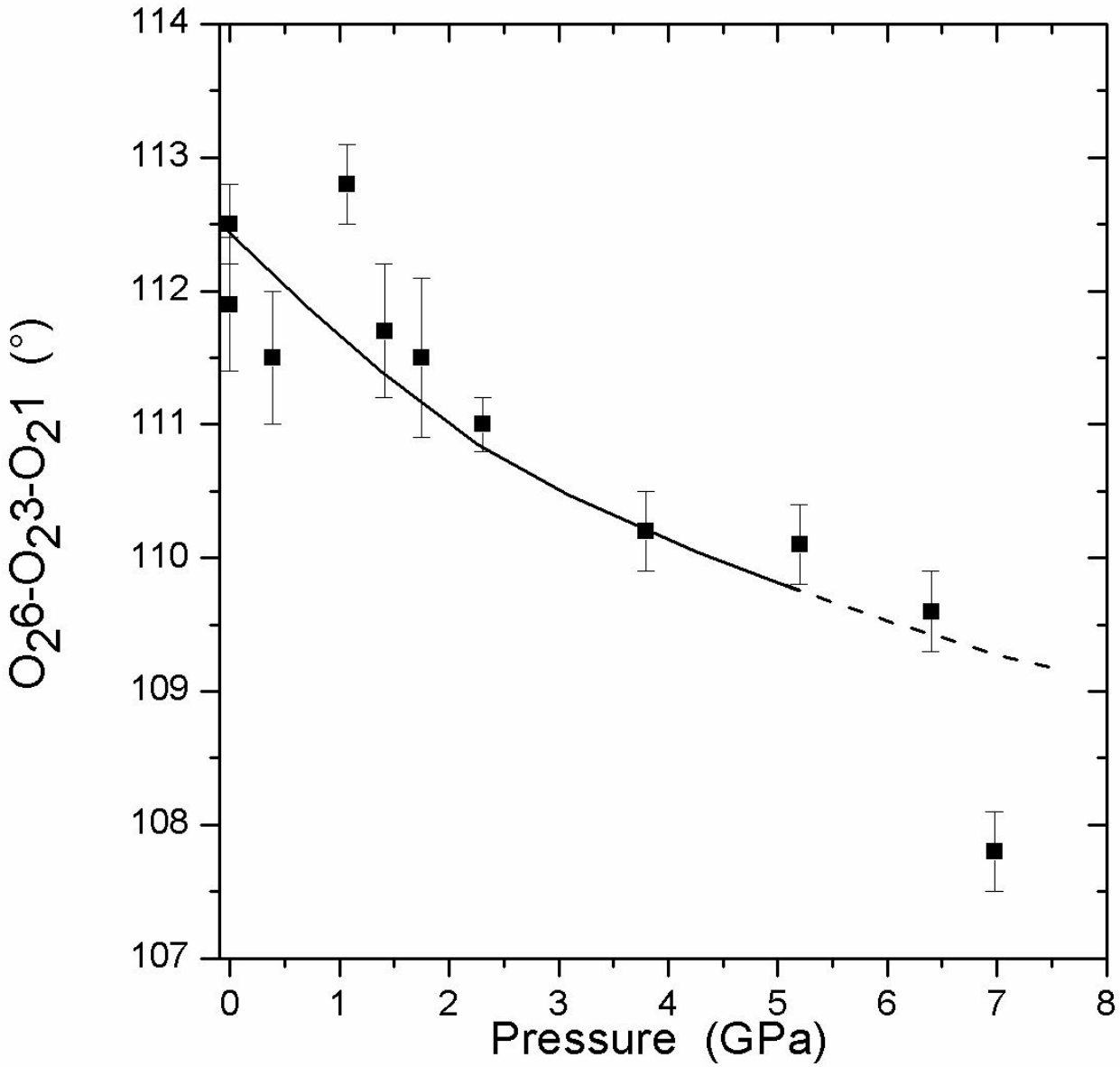
114
113
112
111
110
109
108
107
0
1
2
3
4
5
6
7
8
Pressure (GPa)
O26-O23-O21 (°)

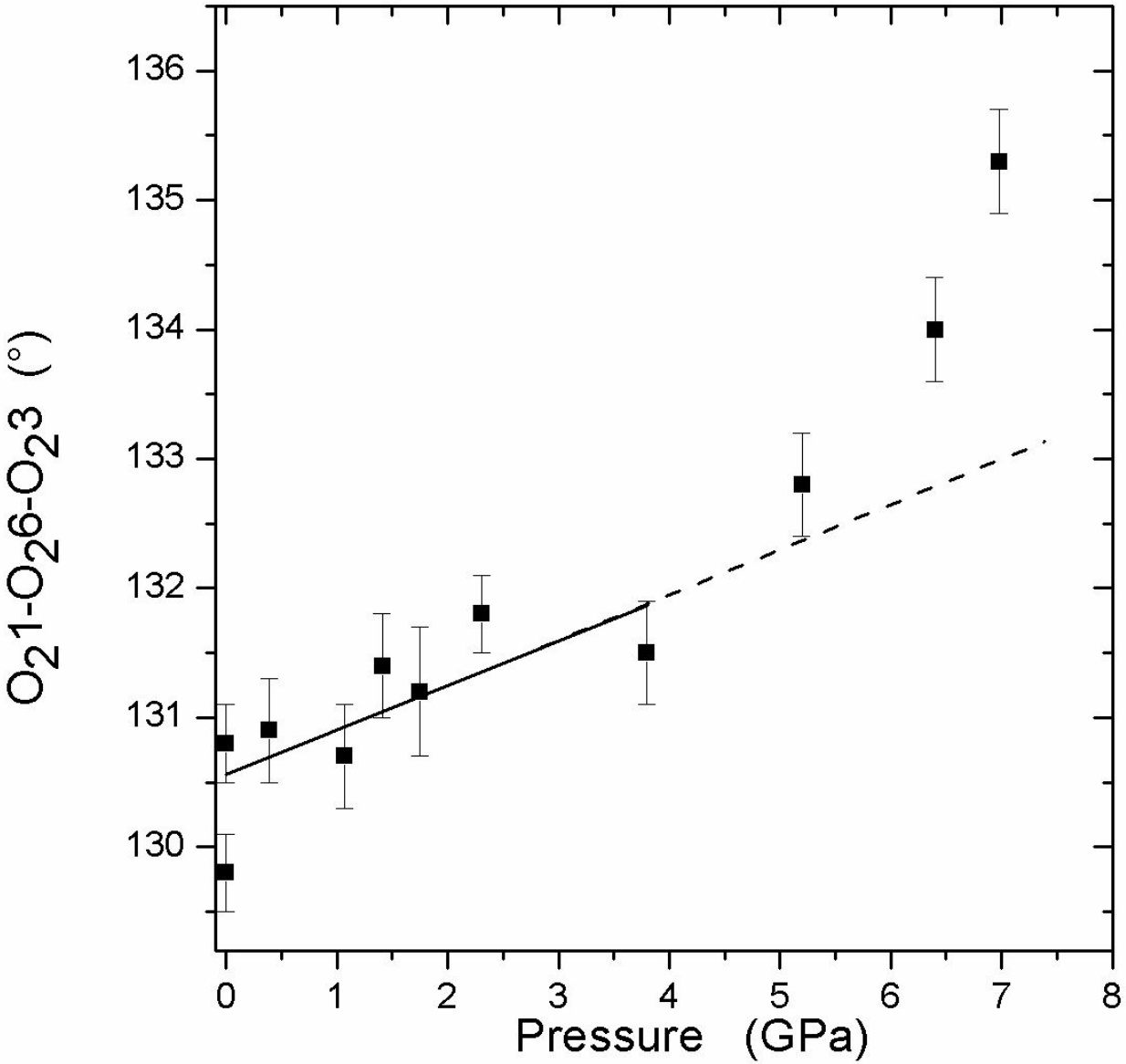
O21-O26-O23 (°)
136
135
134
133
132
131
130
0
1
2
3
4
5
6
7
8
Pressure (GPa)